Title

Electronic Structure of the Primary Electron Donor P 700 +• in Photosystem I Studied by Multifrequency HYSCORE Spectroscopy at X- and Q-Band

Journal

The Journal of Physical Chemistry B, 125(1)

ISSN

1520-6106

Authors

Chestnut, Melanie M
Milikisiyants, Sergey
Chatterjee, Ruchira
et al.

Publication Date

2021-01-14

DOI

10.1021/acs.jpcb.0c09000

Peer reviewed

Electronic Structure of the Primary Electron Donor $P_{700}^{+\bullet}$ in Photosystem I Studied by Multifrequency HYSCORE Spectroscopy at X- and Q-Band

Melanie M. Chestnut,[†,‖] *Sergey Millikisiyants,* [†,‖] *Ruchira Chatterjee,*[‡] *Jan Kern,* [‡] *and Alex I. Smirnov*[*, †]

[†]Department of Chemistry, North Carolina State University, 2620 Yarbrough Drive, Raleigh, North Carolina 27695-8204, United States

[‡]Molecular Biophysics and Integrated Bioimaging Division, Lawrence Berkeley National Laboratory, Berkeley, California 94720, United States

ABSTRACT

The primary electron donor P_{700} of the photosystem I (*PS*I) is a heterodimer consisting of two chlorophyll molecules. A series of electron transfer events immediately following the initial light excitation leads to a stabilization of the positive charge by its cation radical form, $P_{700}^{+\bullet}$. The electronic structure of $P_{700}^{+\bullet}$ and, in particular, its asymmetry with respect to the two chlorophyll monomers is of fundamental interest and is not fully understood up to this date. Here, we apply multi-frequency X- (9 GHz) and Q-band (35 GHz) hyperfine sublevel correlation (HYSCORE) spectroscopy to investigate the electron spin density distribution in the cation radical $P_{700}^{+\bullet}$ of *PS*I from a thermophilic cyanobacterium *Thermosynechococcus elongatus.* Six ^{14}N and two ^{1}H distinct nuclei have been resolved in the HYSCORE spectra and parameters of the corresponding nuclear hyperfine and quadrupolar hyperfine interactions were obtained by combining the analysis of HYSCORE spectral features with direct numerical simulations. Based on a close similarity of the nuclear quadrupole tensor parameters, all the resolved ^{14}N nuclei were assigned to six out of total eight available pyrrole ring nitrogen atoms (*i.e.*, four in each of the chlorophylls), providing the direct evidence of spin density delocalization over the both monomers in the heterodimer. Using the obtained experimental values of the ^{14}N electron-nuclear hyperfine interaction parameters, the upper limit of the electron spin density asymmetry parameter is estimated as $R_{\mathrm{A/B}}^{\mathrm{upper}} = 7.7 \pm 0.5$ while a tentative assignment of ^{14}N observed in the HYSCORE spectra yields $R_{\mathrm{B/A}} = 3.1 \pm 0.5$.

INTRODUCTION

The photosystem I (*PS*I) is an integral membrane pigment-protein complex found in many photosynthetic organisms including including cyanobacteria, algae, and higher plants and shares many similarities with the reaction center of green sulfur bacteria as both are the type I reaction centers plants.[1-7] The overall function of *PS*I involves capturing and transferring solar light energy to catalyze the oxidation of the plastocyanin/cytochrome c_6 and the reduction of ferrodoxin/flavodoxin proteins, which provide electrons for a variety of chloroplast reactions, including NADPH production, nitrate assimilation, and fatty acid desaturation.[8]

The electron transfer in *PS*I starts with light-induced oxidation of the P_{700} pigment located in the structurally similar *PsaA* and *PsaB* proteins which span the thylakoid membrane.[9] P_{700} is a heterodimer consisting of two chlorophyll molecules denoted as P_A and P_B by referring to their location in the *PsaA* and *PsaB* subunits, respectively. Structurally, P_B is a chlorophyll *a* (*Chl a*) and P_A is a $C13^2$-epimer of the chlorophyll *a* (*Chl a*'). The electron transfer proceeds sequentially via a series of acceptors conventionally called A_0, A_1, F_X, F_A, and F_B.[9] The central role of P_{700} in the function of *PS*I is attributed to its location at the interface of the excitation transfer from the light harvesting system and the electron transfer in the reaction center as well as its unique redox properties, which are distinct from all the other chlorophylls.[10] The reduction potential of the electronically excited P_{700} is ≈ - 1.2 V making it possibly the most reducing chemical species in nature.[11] While some of the reports debated the nature of the primary electron donor,[12-14,15-19] it is the P_{700} special pair that localizes the positive charge, thus, stabilizing the charge-separated state required for the consequent reduction of ferrodoxin/flavodoxin proteins.

Given the central role P_{700} plays in the redox activity of *PS*I, its chemical and electronic structures have been the focus of intense research for several decades.[11] We note that although the chemical composition of P_{700} as a Chl *a*/Chl *a*' coplanar heterodimer has been unambiguously confirmed by high resolution X-ray crystallography of cyanobacterial *PS*I,[20] the electronic structure of P_{700} in its singlet, triplet, and radical states still remains the subject of much interest and discussions. While several experimental spectroscopic techniques have been proven to be informative in unraveling the electronic structure of the primary donor,[11] electron paramagnetic resonance spectroscopy (EPR) was found to be particularly useful due to the paramagnetic nature of both the triplet and the cation radical forms of P_{700}.

The triplet state $^3P_{700}$ is usually formed after a charge recombination when the reduction of F_X and A_1 results in the electron transfer being blocked to continue beyond the first acceptor A_0.[21-22] This net S=1 electron spin state is characterized by a magnetic dipolar interaction between the two unpaired electronic spins described in terms of D and E parameters of the zero field splitting (ZFS).[23] At magnetic fields $B_0 \approx 3,200$ G of X-band (9 GHz) EPR, the anisotropy of the Zeeman term is typically much smaller than the magnitude of the ZFS interaction (*i.e.*, $\Delta g \gamma_e B_0 \ll D$). Under such conditions the principal components of the $\boldsymbol{g}$-matrix are unresolved and the EPR spectra are dominated by the ZFS features. Thus, EPR characterization of $^3P_{700}$ has been primarily focused on measurements of D and E parameters of ZFS[23] and a comparison with those of monomeric chlorophyll.[24-25] Detailed analysis of the $\boldsymbol{g}$-matrix became possible with development of High Field / High Frequency (HF) EPR. Specifically, analysis of $\boldsymbol{g}$-matrix and ZFS components obtained from experimental time-resolved D-band (130 GHz) polarized EPR spectra of $^3P_{700}$ demonstrated that the electronic structure of the triplet state is very different from that of the monomeric *Chl a*.[26] While such studies were proven to be informative, the data

on ***g***-matrix and ZFS parameters alone appear to be insufficient for arriving at unambiguous conclusions regarding the electron spin density delocalization over the two monomeric chlorophylls of $^3P_{700}$. For example, Poluektov concluded that the observed ***g***-matrix and ZFS parameters can be rationalized either by a delocalized electronic character of the $^3P_{700}$ state or by a heteromeric model of the primary donor in *PS*I.[26]

More extensive research on the electronic structure of P_{700} has been conducted by using the cation radical form of the primary electron donor, $P_{700}^{+\bullet}$.[11] Specifically, HF EPR studies of frozen detergent-solubilized $P_{700}^{+\bullet}$ at *ca*. 325 and 437 GHz demonstrated excellent spectral resolution of all three ***g***-matrix principle components[27] while the orientation of the ***g***-matrix with respect to the molecular frame has been derived from single crystal Q-band (35 GHz)[28] and W-band (94 GHz)[29] EPR studies. The magnitude of the ***g***-matrix anisotropy of $P_{700}^{+\bullet}$ has been found to be nearly identical to that of the monomeric *Chl a*, indicating that most of the electron spin density is carried by of one of the chlorophyll subunits. In contrast, unusual temperature dependence of the ***g***-matrix is more consistent with the dimeric nature of $P_{700}^{+\bullet}$.[30] HF EPR at 330 GHz combined with site-directed mutagenesis pointed to most of the spin density being carried out by P_B, the *Chl a* molecule located in the B branch of *PS*I.[31] While all these HF EPR studies demonstrated a significant progress in understanding the electronic structure of $P_{700}^{+\bullet}$, the complex relationship between the ***g***-matrix anisotropy and the distribution of the electron spin density prevented the researchers from drawing final conclusions on the spin density delocalization over the two dimers.

Further information on the electron spin delocalization in paramagnetic molecules can be obtained from measuring isotropic components of the electron-nuclear hyperfine interactions that

are directly related to the spin density on magnetic nuclei. For both *Chl a* and *Chl a*' the electron spin density can be conveniently probed by naturally abundant magnetic nuclei such as several ^{1}H and the four pyrrole ring ^{14}N nuclei, which are commonly denoted N_I through N_{IV} based on the numbering of the corresponding rings (Scheme 1). Such measurements would also be indicative whether the electron spin density is partially transferred to the two axial ligands, $HisA_{680}$ and $HisB_{660}$, which are coordinating P_A and P_B respectively.

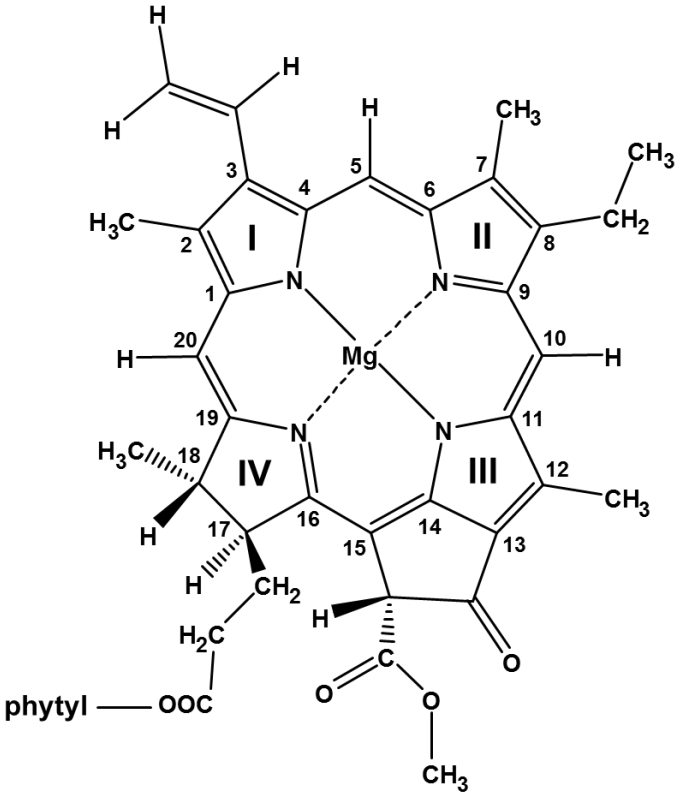

Scheme 1. Structure of the chlorophyll *a* (*Chl a*) with IUPAC numbering of molecular positions.

While spectral features from nuclear hyperfine coupling interactions in $P_{700}^{+\bullet}$ remain unresolved in field-swept EPR spectra, the data on such interactions can be obtained by a number of pulse

EPR and/or double-resonance techniques[11, 32] with electron nuclear double resonance (ENDOR) and electron spin echo envelope modulation (ESEEM) spectroscopies being among the most successful methods.[11, 32-33] Unfortunately, a combination of the bulky conjugated π-system with an abundance of ^{1}H and ^{14}N magnetic nuclei has proven to be the major obstacle for resolving the individual hyperfine contributions of the P_A and P_B halves of the P_{700} heterodimer. Furthermore, for $P_{700}^{+\bullet}$ samples prepared as frozen solutions, the resulting orientational disorder makes the interpretation of ENDOR and ESEEM spectra especially difficult and prone to errors. For these reasons, the most accurate measurements of the hyperfine interactions in $P_{700}^{+\bullet}$ to this date were obtained from single crystals of *PS*I studied at multiple orientations with respect to the external magnetic field.[10] The full set of parameters of the hyperfine tensor including all the principle values and the tensor orientation with respect to the molecular frame were accurately measured for three types of methyl protons of the P_B molecule.[10] Based on a comparison with the monomeric *Chl a*, it was argued that at least 85% of the electron spin density is carried by the P_B molecule.[10] On the other hand, some of the detected smaller hyperfine couplings were tentatively assigned to P_A, leading to an estimate of the spin density distribution between the two halves of the dimer between 75:25 and 70:30.[34] ESEEM experiments with *PS*I single crystals samples revealed the coupling of the electronic spin to five different ^{14}N nuclei and yielded accurate measurements of the corresponding nuclear quadrupole parameters K and η. These results provided an indirect evidence of the electron spin density being carried by both P_A and P_B.[35] Unfortunately, electron-nuclear hyperfine couplings, which are more informative for deriving electron spin density delocalization, remained unresolved even for the single crystals, owing to the extreme complexity and insufficient resolution of ESEEM spectra that are one-dimensional in nature.[35]

To summarize, based on the authors' knowledge, no unambiguous detection of electron spin density on any of the nuclei belonging to the P_A side has been achieved to this day, leaving the question of the dimeric *vs*. monomeric nature of the cation radical $P_{700}^{+\bullet}$ to be the subject of further discussions and investigations. Methods alternative to EPR, such as photo-CIDNP[36-37] and FTIR[38-39] have been applied in attempts of obtaining the clear answer but resulted in contradictive models of $P_{700}^{+\bullet}$ ranging from a fully monomeric radical species to the equal contributions from both chlorophylls P_A and P_B.[37-38, 40-41]

Here we report on a multi-frequency (X- and Q-band) hyperfine sublevel correlation spectroscopy (HYSCORE) investigation of the electronic structure of $P_{700}^{+\bullet}$ in *PS*I solubilized from thermophilic cyanobacterium *Thermosynechococcus elongatus*. As a 2D-method, HYSCORE dramatically reduces the spectral crowding of the 1D techniques of ESEEM and ENDOR,[42] thus, allowing for detection of ^{14}N hyperfine couplings with high resolution. Here a combination of the 4-pulse[42] and 6-pulse[43] sequences is chosen to extend the sensitivity range of the HYSCORE spectroscopy. A special attention is paid to distinguish between the spectral contributions attributed to weakly interacting nuclei and potential artifacts caused by the experimental imperfections.

2. EXPERIMENTAL SECTION

Sample Preparation. Cultivation of *Thermosynechococcus elongatus* and extraction of *PS*I were performed as reported previously.[44] *PS*I was purified by a column packed with Toyo Pearl DEAE 650 S (GE Healthcare, Germany), where *PS*I was eluted at 20 mM 2-(*N*-morpholino)ethanesulfonic acid (MES) NaOH buffer at *p*H 6.0, 5% glycerol (v/v), 20 mM $CaCl_2$ and 0.02% *n*-dodecyl β-D-maltoside (DDM) (w/v), 55 mM $MgSO_4$. The final *PS*I protein

solution (6 mM chlorophyl concentration) was prepared in a buffer containing 20 mM MES-NaOH, pH 6.0, 5% glycerol (v/v), 20 mM $CaCl_2$ and 0.02% DDM (w/v), 60 mM $MgSO_4$. $P_{700}^{+\bullet}$ was generated chemically by incubating the solution with 20 mM of $K_3\left[Fe(CN)_6\right]$ for 10 min.

EPR Spectroscopy. Pulsed EPR experiments were carried out using an ELEXSYS E580 spectrometer (Bruker Biospin, Billerica, MA, USA) equipped with a SuperQFTu bridge for X- (9 GHz) and Q- (35 GHz) band experiments. Both X- and Q-band spectra were acquired at 76 K using a Bruker ER 4118CF flow cryostat cooled with liquid nitrogen. The standard 16-step phase cycling procedure for the 4-pulse HYSCORE and the original 8-step phase cycling procedure 32 for the 6-pulse HYSCORE[43] were employed.

X-band HYSCORE. For X-band time-domain experiments π/2 (of 10 ns duration) and π (of 20 ns duration) microwave pulses at 9.67 GHz were generated using an E-580–1030 1 kW TWT amplifier. Aqueous samples were drawn into 3 × 4 mm (i.d. × o.d.) quartz tubes (Wilmad-LabGlass, Vineland, NJ, USA), frozen by immersing into liquid nitrogen, and rapidly transferred into a precooled ER 4118X-MD5W dielectric resonator. All HYSCORE spectra were measured by setting the magnetic field to *ca*. 3,450 G to match the maximum of the echo-detected field-swept spectra (Figure 1A).

Initial separation between the second and the third pulses for 4-pulse HYSCORE) as well as between the third and the fourth pulses for 6-pulse HYSCORE was 24 ns. Initial separation between the third and the fourth pulses for 4-pulse HYSCORE as well as between the fourth and the fifth pulses for 6-pulse HYSCORE was 34 ns. This 10 ns increase in the pulse separation was applied to account for the difference in length between π/2 and π pulses. Both pulse separations were incremented by 16 ns to obtain 2D experimental time-domain spectra consisting

of 300×300 data points. All other inter-pulse separations for both the 4-pulse and 6-pulse HYSCORE experiments are provided in the Results and Discussion section.

Q-band HYSCORE. For Q-band time-domain experiments π/2 (of 10 ns duration) and π (of 18 ns duration) microwave pulses at 33.801 GHz were generated using a 10 W AmpQ solid state power amplifier. Aqueous samples were drawn into the standard 1.2 × 1.6 mm (i.d. × o.d.) quartz tubes (Wilmad-LabGlass), frozen by immersing into liquid nitrogen, and rapidly transferred into a precooled Q-band EN 5107D2 resonator. All HYSCORE spectra were measured by setting the magnetic field of *ca*. 1,205 G to match the maximum of the echo detected field-swept spectra (Figure 1B).

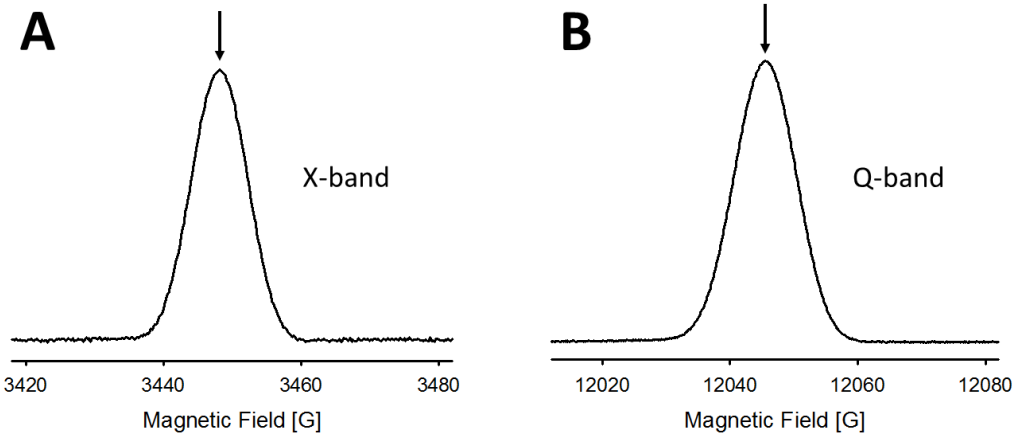

Figure 1. Echo-detected field-swept spectra of the primary electron donor $P_{700}^{+\bullet}$ in the oxidized state at X- (**A**) and Q-band (**B**) EPR frequencies, $T \approx 76$ K. The arrows indicate the magnetic field positions for the respective HYSCORE experiments. See text for details.

Initial separation between the second and the third pulses for 4-pulse HYSCORE as well as between the third and the fourth pulses for 6-pulse HYSCORE was 22 ns. Initial separation between the third and the fourth pulses for 4-pulse HYSCORE as well as between the fourth and the fifth pulses for 6-pulse HYSCORE, was 30 ns. This 8 ns increase in the pulse separation was

applied to account for the difference in length between π/2 and π pulses. Both pulse separations were incremented by 16 ns to obtain 2D experimental time-domain spectra consisting of 300 × 300 data points. All other inter-pulse separations for both the 4-pulse and 6-pulse HYSCORE were determined by the locations of the blind-spots and are provided in the Results and Discussion section.

Signal processing and analysis of HYSCORE spectra. 2D frequency-domain HYSCORE spectra were obtained from the experimental time-domain data by completing the following consecutive steps. (1) Firstly, 2D data were least-squares fitted to 3rd order polynomials that was consequently subtracted from the data in both dimensions as a 2D baseline. (2) Secondly, a Hamming function was employed to reduce the side lobe artifacts. Apodization was applied sequentially to each of the dimensions. (3) Thirdly, 2D time domain signal was zero filled to yield a 2048 × 2048 matrix. (4) Finally, the resulting time-domain data were subjected to a fast Fourier transform (FFT), converted into the absolute values, symmetrized by taking an average with respect to the two matrix indices, and plotted using the "contour" function of the Matlab R2016a software (MathWorks, Natick, MA).

All the ^{14}N-HYSCORE spectra were simulated using Easyspin-5.2.20 software package[45] running with Matlab R2016a. Estimates of the ^{14}N hyperfine coupling parameters and the corresponding errors were determined by comparing the locations and shapes of the (double quantum) - (double quantum) ridges of the simulated and the experimental spectra. As an approximation, electron-nuclear hyperfine coupling $\boldsymbol{A}$ tensor was assumed to be axial (*i.e.*, two of the principal components were set to be equal). During the simulations, the orientation of the electron-nuclear hyperfine coupling $\boldsymbol{A}$ tensor, defined by its principal values $\left[A_{xx}, A_{yy}, A_{zz} \right]$, was set to be parallel to the orientation of the traceless nuclear quadrupole tensor with the principal

values $\left[-K(1-\eta),-K(1+\eta),2K\right]$. During the simulations, the direction of the axial electron-nuclear hyperfine coupling component $A_{\|}$ was interchanged between all three possible orientations, *i.e.*, either $A_{\|}=A_{xx}$, $A_{\|}=A_{yy}$, or $A_{\|}=A_{zz}$, and a tensor orientation yielding the best agreement between the simulation and the experiment was chosen.

Proton hyperfine coupling parameters were obtained from experimental ^{1}H-HYSCORE spectra using a linear analysis procedure described in detail elsewhere.[46]

3. RESULTS AND DISCUSSION

3.1. Field Swept Echo-Detected EPR Spectra of $P_{700}^{+\bullet}$

Echo-detected field-swept X- and Q-band EPR spectra of the dark-adapted state of *PS*I from thermophilic cyanobacterium *Synechococcus elongatus* measured at T = 76 K in presence of 20 mM $K_3\left[Fe(CN)_6\right]$ are shown in Figures 1A and B, respectively. Both spectra reveal a single EPR line without any other resolved features. The line was centered at $g\approx2.0025$ as one expects for the $P_{700}^{+\bullet}$ species.[47] The observed ≈ 10 G linewidth (full width at half height) at X-band is slightly larger than ≈7 G measured by continuous wave (CW) EPR[47] because of an additional broadening caused by short pulses with the excitation bandwidth comparable to the linewidth. We note that the echo-detected EPR spectra shown in Figure 1 are free of unwanted contributions, such as EPR-active species A_0^-, A_0^-, and Fe^{3+} of ferricyanide, all of which would result in much broader EPR spectral features.[9] While Fe^{3+} ions are abundant in the sample, the very fast electron spin relaxation at T = 76 K prevented an observation of such ions by pulsed EPR. Additionally, the presence of A_0^- and A_0^- species is not expected at these experimental conditions.[10] The echo-detected X- and Q-band EPR spectra yielded the values of magnetic

fields for the maximal echo intensities (indicated by arrows in Figure 1) that were then used for measurements of the HYSCORE spectra.

3.2. X-Band 4-pulse HYSCORE of $P_{700}^{+\bullet}$

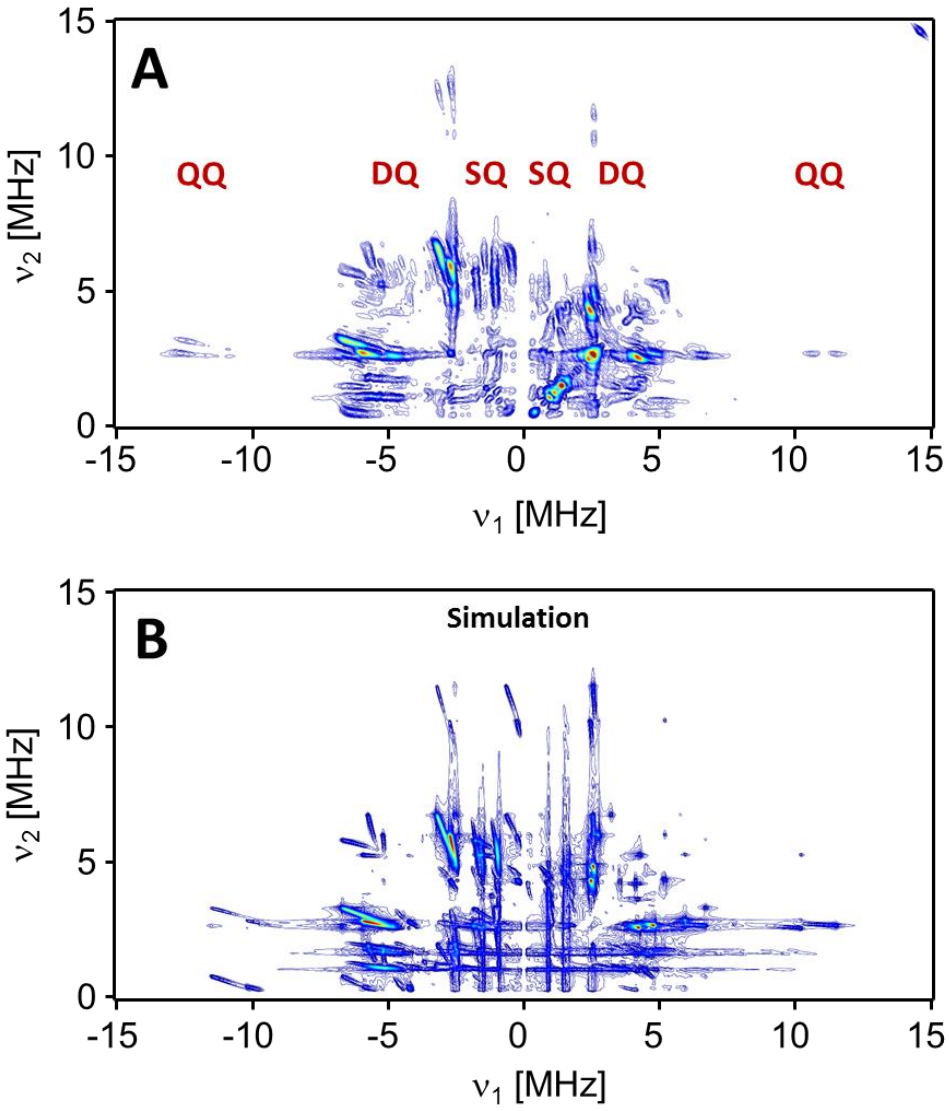

Figure 2. (**A**) Experimental 4-pulse X-band HYSCORE spectrum of $P_{700}^{+\bullet}$ (T≈76 K) measured with a delay of 120 ns between the first π/2 and the second π/2 microwave pulses. Spectral

regions corresponding to multi-quantum nuclear transitions are marked with red text. (**B**) Simulated spectrum. See text for details including an identification of specific transitions.

The (+,+) and (-,+) quadrants of the 4-pulse HYSCORE spectrum of $P_{700}^{+\bullet}$ measured at X-band are shown in Figure 2A. The delay between the first π/2 and the second π/2 pulses was 120 ns, which corresponds to the blind spots at $n \times 8.3$ MHz with n being a positive integer (n = 0, 1, 2…). To ensure that no additional signals are hidden due to these blind spots, 4-pulse HYSCORE spectra with 100 ns (blind spots at n×10 MHz) and 140 ns (blind spots at n×7.1 MHz) delays between the first and second pulses were also measured (not shown).

The HYSCORE spectrum shown in Figure 2A exhibits a rather complex pattern of features arising from multiple ^{14}N nuclei and a single structureless low intensity peak at (14.7, 14.7) MHz due to ^{1}H. The location of each individual cross-peak depends on the relative orientation of the molecular frame with respect to the external magnetic field. The random orientations of molecules in frozen solutions further complicates the spectrum by averaging over all possible angles with respect to the magnetic field. Such an averaging leads to a formation of specific 2D patterns, which are commonly called HYSCORE ridges. Approximate locations of the spectral regions of the single quantum (SQ), double quantum (DQ), and quadruple quantum (QQ) nuclear transitions are marked in Figure 2A by the corresponding abbreviations. The complex pattern observed in the HYSCORE spectra consists of ridges reflecting correlations of various quantum transitions (*e.g.*, SQ-SQ, SQ-DQ, DQ-DQ, *etc*.), as well as some of their combination peaks. The combination peaks arise mainly from a factorization of the HYSCORE signal when an unpaired electron spin interacts simultaneously with more than one magnetic nucleus. In addition, non-correlated features (pseudo 2D cross-peaks) located on the main diagonals ($\nu_1 = \nu_2$ for the (+,+)

quadrant and $\nu_1 = -\nu_2$ for the (-,+) quadrant) mainly caused by an incomplete inversion of the spins by the third π-pulse, are also observed. The incomplete inversion by the π-pulse (estimated efficiency of ≈70%) causes the 3-pulse ESEEM signal to "leak" into the detected 2D time domain signal. The effective time coordinate of the 3-pulse ESEEM is equal to the sum of the two HYSCORE time coordinates and, therefore, yields the peaks appearing on the main diagonals. The sharp non-correlated signals correspond to the ν_0, ν_-, ν_+, and ν_{DQ} peaks dominating the 1D 3-pulse ^{14}N-ESEEM spectrum at the so-called "cancellation condition", *i.e.* when the magnitude of the electron nuclear hyperfine coupling interaction A is about twice as large as the ^{14}N Larmor frequency ν_I.[48-49] When the cancellation condition $A = 2\nu_I$ is exactly satisfied, the spectral position of the peaks is determined by only the quadrupole interaction parameters K and η: $\nu_0 = 2K\eta$, $\nu_- = 3K(1-\eta)$, $\nu_+ = 3K(1+\eta)$, and $\nu_{DQ} = 2K(3+\eta^2)$.[48] Being the pseudo 2D peaks, their coordinates are (ν_0,ν_0), (ν_-,ν_-), (ν_+,ν_+), and (ν_{DQ},ν_{DQ}), respectively. While these non-correlated 3-pulse ESEEM peaks, together with the ridges corresponding to the DQ-DQ transitions, dominate the crowded HYSCORE spectrum (Figure 2A), their high intensities are caused by different reasons. When the cancellation condition $A = 2\nu_I$ is fulfilled for a ^{14}N nuclear spin, the 3-pulse echo intensity increases dramatically yielding intense sharp peaks at ν_0, ν_-, and ν_+ frequencies – all corresponding to the single quantum transitions. A somewhat less intense peak at ν_{DQ} will also appear. The latter peak is caused by double quantum transitions within the electron spin manifold at frequencies at which the electron-nuclear hyperfine coupling and the nuclear Zeeman interactions cancel each other. The spectral positions of the cross-correlated DQ-DQ peaks exhibit a rather weak dependence on the orientation of the molecular frame with respect to the magnetic field because of a typically

modest anisotropy of the electron nuclear hyperfine coupling interaction. Therefore, averaging over all possible molecular orientations would only moderately shift these spectral peaks and, thus, give rise to some intense ridges in the HYSCORE spectra. The average frequencies ν_1^{DQ} and ν_2^{DQ} of the ridges in these 2D spectra are approximately given by the following equations:[48]

$$\nu_1^{DQ} \approx \pm 2\sqrt{\left(\nu_I + A/2\right)^2 + K^2\left(3+\eta^2\right)}\ , \qquad \nu_2^{DQ} \approx \pm 2\sqrt{\left(\nu_I - A/2\right)^2 + K^2\left(3+\eta^2\right)}, \quad (1)$$

where the + or - signs are determined by the quadrants of a HYSCORE spectrum in which the transition peaks appear and A is a secular component of the hyperfine coupling tensor $\boldsymbol{A}$ determined mainly by its isotropic part. The shape of the ridges is determined by the $\boldsymbol{A}$-tensor anisotropy.

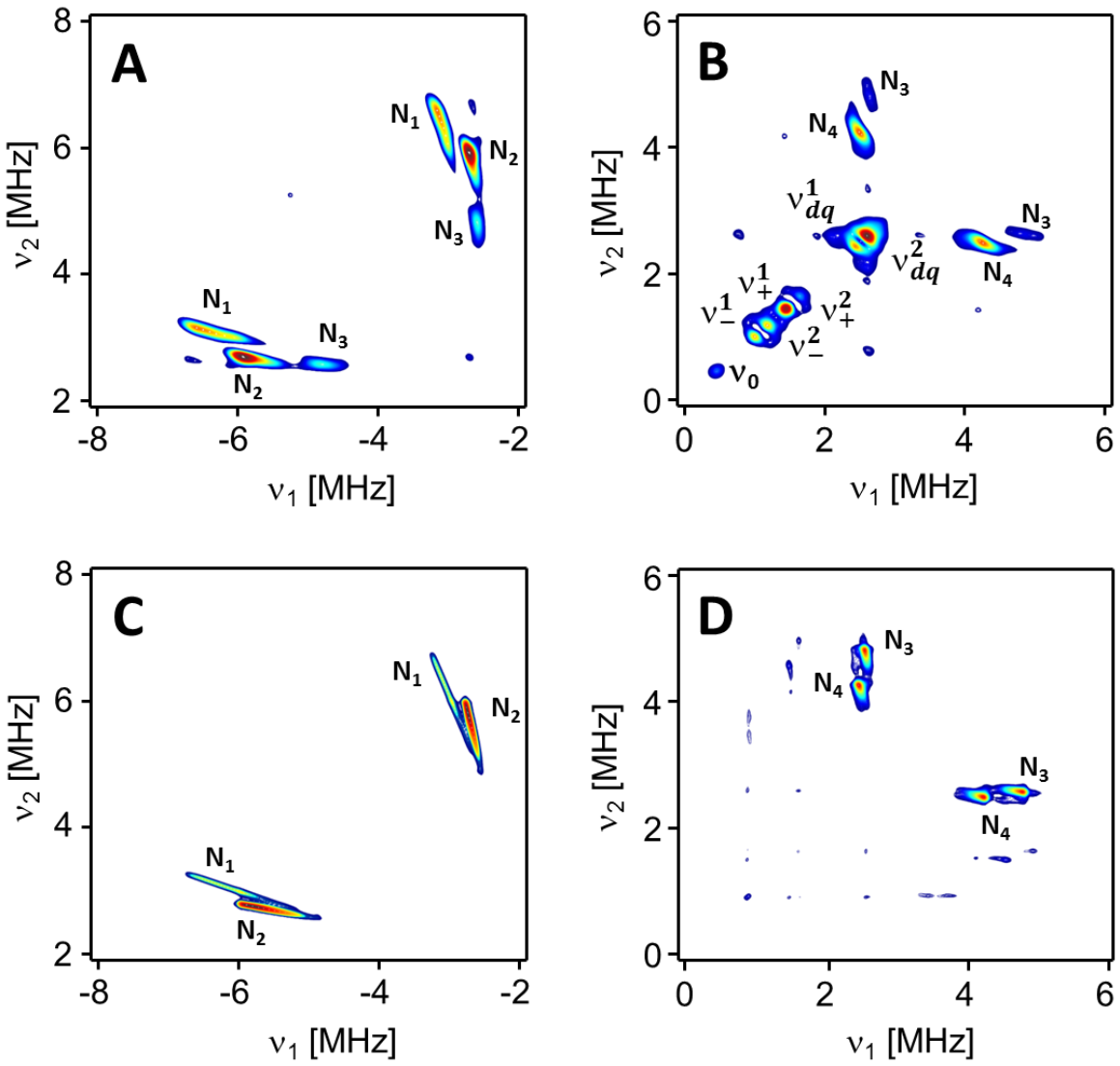

Figure 3. Zoomed-in regions of the experimental and simulated X-band HYSCORE spectra of $P_{700}^{+\bullet}$ (Figure 2). The experimental (-,+) quadrant region with DQ-DQ features (**A**) is compared with the simulated N_1-N_3 ridges **(C**). The experimental (+,+) quadrant region with DQ-DQ features (**B**) is compared with the simulated N_3-N_4 ridges (**D**). See text for the assignment of the spectral features.

While the spectral complexity makes an unambiguous interpretation of the observed HYSCORE a rather difficult task, the spectral locations of the non-correlated 3-pulse ESEEM

features and especially the DQ-DQ ridges provide valuable information on the electron - nuclear spin interactions in the $P_{700}^{+\bullet}$ spin system.

Figure 3A shows two zoomed-in regions of the HYSCORE spectrum (Figure 2) corresponding to the DQ-DQ and 3-pulse ESEEM features by using a higher minimal level in the contour map to remove nearly all other spectral contributions. At least three types of DQ-DQ ridges are clearly resolved in the (-,+) quadrant and two in the (+,+) quadrant. Seven 3-pulse ESEEM features denoted as ν_0, ν_-^1, ν_-^2, ν_+^1, ν_+^2, ν_{DQ}^1, and ν_{DQ}^2 are resolved on the main diagonal of the (+,+) quadrant (Figure 3B). The positions of these peaks for each of the resolved DQ ridges provided for initial estimates of the hyperfine parameters *A*, *K*, and η. While the electron-nuclear hyperfine coupling constants *A* are expected to vary significantly (*i.e.*, from *ca*. 1 to 5 MHz), the quadrupole tensor parameters of all the observed ^{14}N nuclei must be very similar.

We interpret the observed HYSCORE spectrum as a superposition of individual contributions from four different of ^{14}N nuclei: N_1, N_2, N_3, and N_4. The appearance of the DQ-DQ ridges attributed to N_1 and N_2 only in the (-,+) quadrant (Figure 3A) indicates that their electron-nuclear couplings *A* exceeds the double of the nuclear Larmor frequency, *i.e.*, $A > 2\nu_I$. On the contrary, the appearance of the DQ-DQ ridges of N_4 only in the (+,+) quadrant (Figure 3B) indicates the opposite, *i.e.*, $A < 2\nu_I$. Out of four ^{14}N nuclei only N_3 has a pronounced DQ-DQ intensity in both quadrants; thus, $A \approx 2\nu_I$. The observed seven 3-pulse ESEEM features indicate two types of the quadrupole couplings having (nearly) identical values of *K* and η. The 3-pulse features are most likely attributed to N_3 and N_4, since, to the authors experience, no significant 3-pulse

ESEEM features (except sometimes the (ν_{DQ},ν_{DQ}) feature) are observed in the HYSCORE spectrum when $A > 2\nu_I$ (*i.e.*, whenever the DQ-DQ features appear only in the (-,+) quadrant).

Table 1. ^{14}N and ^{1}H hyperfine coupling interaction parameters of $P_{700}^{+\bullet}$ obtained from simulations of the experimental HYSCORE spectrum of Figure 2.

Nucleus	$[A_{\parallel}, A_{\perp}]$, MHz	A_{iso},[a] MHz	K, MHz	H
N_1	[4.1±0.2, 2.1±0.6]	2.8±0.4	0.70±0.05	0.65±0.25
N_2	[3.4±0.2, 1.8±0.5]	2.3±0.3	0.65±0.05	0.70±0.25
N_3	[1.9±0.1, 1.1±0.3]	1.4±0.2	0.70±0.05	0.65±0.25
N_4	[1.5±0.1, 1.0±0.5]	1.2±0.3	0.65±0.05	0.70±0.25
N_5	[0.77±0.05, 0.32±0.10]	0.47±0.07	0.55±0.05	0.85±0.15
N_6	[0.64±0.05, 0.35±0.10]	0.45±0.07	0.62±0.05	0.80±0.20
H_1	[9.9±0.5, 6.6±0.5]	7.7±0.4	-	-
H_2	[8.3±0.4, 5.2±0.4]	6.2±0.3	-	-

[a] A_{iso} was calculated from $[A_{\parallel}, A_{\perp}]$ as $A_{iso} = \frac{1}{3}(A_{\parallel} + 2A_{\perp})$.

The spectral locations of the observed DQ-DQ ridges and the diagonal features all point to very similar quadrupole parameters for all the observed ^{14}N nuclei. This similarity of the quadruple couplings increases spectral crowding and leads to a potential ambiguity of the spectral interpretation. Thus, a further extra care must be taken to avoid the possibilities that (*i*) any of the observed DQ-DQ ridges may be experimental artifacts or (*ii*) originate from the same ^{14}N nucleus, as is the case for N_3. The first (*i*) possibility was ruled out by measuring multiple HYSCORE spectra with different inter-pulse delays and also by using a 6-pulse version of the HYSCORE pulse sequence (see the section below). In all the cases, the same spectroscopic

pattern consisting of 5 DQ-DQ ridges was observed. The second (*ii*) possibility was ruled out by numerical simulations of the ^{14}N-HYSCORE spectrum. Figure 2B shows the best simulated 4-pulse HYSCORE spectrum by assuming four different ^{14}N nuclei contributing to the spectrum and an axial character of their electron-nuclear couplings (*i.e.*, $A_{\|} = A_{xx}$ and $A_{\perp} = A_{yy} = A_{zz}$) with the simulation parameters summarized in Table 1. Zoomed-in regions of the simulated HYSCORE spectrum (Figure 2B) corresponding to the DQ-DQ ridges are shown in the Figures 3 C and D. We note that because of the pulse imperfection and other artifacts present in the spectra, the goal of the simulations was to reproduce positions of the most intense and reliable ridges formed by DQ-DQ cross-peaks. In this respect the Figure 3 demonstrates a satisfactory agreement between the simulations and the experiment for all the ridges corresponding to N_1, N_2, N_3, and N_4 ^{14}N nuclei.

A further verification of the assignment of the observed DQ-DQ ridges to N_1-N_4 ^{14}N nuclei and the assumption regarding the similarity of their quadrupolar parameters K and η was obtained from constructing a symmetrized HYSCORE spectrum (Figure 4), which could be obtained, for example, by (*i*) taking the (-,+) quadrant of the experimental HYSCORE spectrum (Fig.2), (*ii*) inverting the sign of the ν_1 frequency axis, and (*iii*) adding such an inverted quadrant to the (+,+) quadrant. The symmetrized spectrum reveals four clearly resolved pairs of DQ-DQ ridges arising from N_1-N_4 nuclei. A dashed line in Figure 4 shows possible positions of the DQ-DQ cross-peaks obtained from Eqs.(1) by fixing the quadrupolar parameters to K=0.65 MHz and η=0.7 and only varying the electron-nuclear hyperfine coupling parameter A. Examination of the Fig.4 reveals that the positions of all the four pairs of DQ-DQ ridges closely fall onto the half-circular dashed line given by Eqns.(1), thus, verifying the origins of the peaks and the

assumption of approximately the same quadrupole interaction parameter for the N_1-N_4 ^{14}N nuclei.

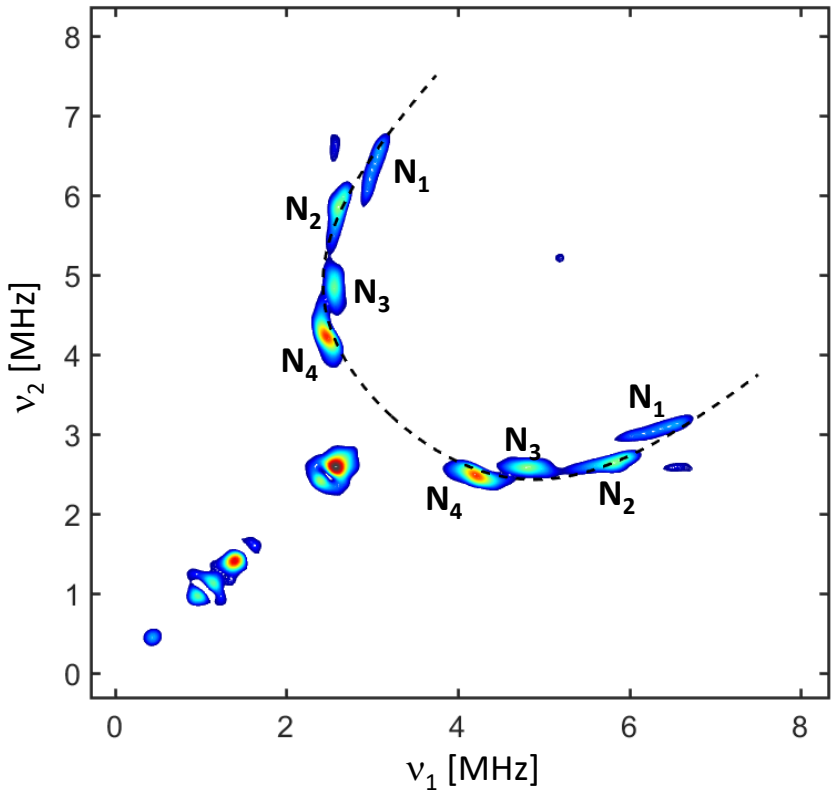

Figure 4. A symmetrized HYSCORE quadrant constructed from the experimental 4-pulse X-band HYSCORE spectrum of $P_{700}^{+\bullet}$ measured with a delay of 120 ns between the first π/2 and the second π/2 microwave pulses. The spectrum was obtained by adding together the experimental (+,+) quadrant and the (-,+) quadrant after inverting the sign of the ν_1 frequency axis. The dashed line represents possible positions of the DQ-DQ cross-peaks calculated from Eqns. (1) by varying by varying the electron-nuclear hyperfine coupling parameter A and keeping the quadrupolar parameters fixed to K=0.65 MHz and η=0.7.

Overall, a comparison of the simulated and experimental HYSCORE spectra in Figure 2 together with the analysis of the symmetrized spectrum of Figure 4 demonstrates that a reasonably good agreement was achieved. Positions of the DQ-DQ ridges were reproduced with high accuracy while the exact shape of the ridges in the experimental spectrum was clearly affected by the pulse imperfections, which were not accounted for in the numerical analysis. The close agreement in the positions of the DQ-DQ ridges in the experimental and simulated HYSCORE spectra was further verified by an examination of the zoomed-in regions for all the observed ^{14}N nuclei shown as an overlay of contour maps in Figure S1A (Supplemental Information). The only significant deviation was the signal intensity distribution among the N_3 DQ-DQ ridges located in the (-,+) and (+,+) quadrants. The authors observed similar deviations for other spin systems with $A \approx 2\nu_I$ when the pulse imperfections resulted in a notable "intensity shift" towards the (-,+) quadrant as compared to the numerical calculations (not shown, unpublished). Interestingly, a satisfactory agreement between the experimental and simulated HYSCORE spectra requires collinearity of all the electron-nuclear hyperfine tensors. Such a collinearity appears to be reasonable because the major fraction of the electron spin density must be delocalized over the π-orbitals of the two coupled *Chl a* and *Chl a*' molecules.

It is worthwhile to note here that the hyperfine coupling parameters for the pair of the N_1 and N_2 nuclei are significantly larger than for the N_3 and N_4 pair (Table 1). While the hyperfine parameters for the N_3 and N_4 nuclei are about the same, the well resolved N_1 and N_2 ridges in the experimental 4-pulse HYSCORE spectrum indicate some slight but measurable differences in both isotropic and anisotropic parameters of the hyperfine coupling interactions. Based on the magnitude of the hyperfine parameters, it is likely that the N_1 and N_2 nuclei are the ring II and ring III nitrogen atoms of P_B.[50] Then the observed differences in the hyperfine parameters of the

N_1 and N_2 nuclei could serve as a further evidence of slight asymmetry between the spin density. This observation agrees well with the results of the earlier DFT calculations.[50]

No other DQ-DQ ^{14}N ridges could be unambiguously detected in any of the measured 4-pulse HYSCORE spectra. If any other strongly interacting ^{14}N nuclei were present in the spectrum, their approximate location would be determined by Eq. (1) with the quadrupole parameters most likely to be close to those of N_1-N_4, since such a strong hyperfine interaction would only be possible for ^{14}N belonging to the *Chl a* or *Chl a*' pyrrole rings. Based on these considerations we can confidently exclude a possibility of another ^{14}N nucleus interacting stronger than N_1-N_4 because the spectral regions at the potential locations of the corresponding DQ-DQ ridges is "clean" (*i.e.*, free of other contributions except some random noise). The intensities of the DQ-DQ ridges drop gradually with the magnitude of *A*; thus, in order to evade the detection by HYSCORE the magnitude of *A* must be rather large, presumably >10 MHz (or >3.6 G). If such a large hyperfine couplings with I=1 nuclear spins were present, such magnetic interactions would be readily detected by CW EPR spectra of perdeuterated $P_{700}^{+\bullet}$ samples that were shown to have linewidth of just ≈3.3 G.[51] Moreover, no ^{14}N spins interacting stronger than N_1 were observed in the Q-band HYSCORE spectra (see the discussion and figures below), where the condition of the Larmor frequency being about threefold of that at X-band favors the detection of such nuclei.

For ^{14}N nuclei interacting weaker than N_4, the spectral resolution problem appears to be significantly more complex. Specifically, intensities of the DQ-DQ ridges drop rapidly with a decrease in *A*. The spectral region where the potential DQ-DQ cross-peaks from such weakly interacting ^{14}N nuclei could be detected is very crowded by the side lobes of the very intense

DQ-DQ ridges of N_3 and N_4 as well as a rather complex pattern made of numerous combination peaks. Thus, detection of such weakly coupled nuclei would require an application of a method that is more sensitive to the weakly coupled nuclei than the standard 4-pulse HYSCORE sequence.

3.3. X-Band 6-pulse HYSCORE of $P_{700}^{+\bullet}$

One way to search for potentially missing weakly interacting ^{14}N nuclei is to apply a 6-pulse HYSCORE sequence which is known to have much higher sensitivity towards weaker hyperfine couplings and is significantly less prone to the unwanted combinatorial peaks.[43] Figure 5A and B shows selected ranges of the (-,+) and (+,+) quadrants of the 6-pulse HYSCORE spectrum of $P_{700}^{+\bullet}$ measured with the inter-pulse delays of 68 ns (blind spots at n × 14.7 MHz, n=0,1,2…) and 120 ns (blind spots at n × 8.3 MHz, n=0,1,2…) between the first two and the last two microwave pulses, respectively. To avoid a loss of spectral information due to the blind-spot effects, two additional 6-pulse HYSCORE spectra with the corresponding inter-pulse delays of 68 ns and 140 ns (blind spots at n × 7.1 MHz, n=0,1,2…; not shown) and 68 ns and 234 ns (blind spots at n × 4.3 MHz, n=0,1,2…), respectively, were also measured. The low frequency region of the (+,+) quadrant of the latter spectrum is shown in Figure 5C.

All the DQ-DQ ridges observed by 4-pulse HYSCORE spectroscopy are clearly resolved in the 6-pulse HYSCORE spectra. As expected, compared to 4-pulse HYSCORE, a strong suppression effect on the 3-pulse ESEEM diagonal features located in the main diagonal was observed. Such a suppression significantly reduced the “crowding” around the spectral area where the DQ-DQ ridges of weakly interacting ^{14}N nuclei are expected to appear. In contrast to

the 4-pulse HYSCORE, two additional pairs of spectral features are clearly detected and resolved by the 6-pulse experiment. We assign these two pairs of new features to two weakly interacting ^{14}N nuclei labeled as N_5 and N_6. Due to a small intensity of these spectral features, an extra care was taken with respect to the assignment of these signals to two "new" ^{14}N nuclei. The following four alternative possibilities were rigorously considered: (*i*) the features are attributed to random noise and/or some pulse imperfection artifacts, (*ii*) any of the four features represent a combination of other peaks in the spectrum, (*iii*) the features do not correspond to DQ-DQ transitions, and (*iv*) the features are side-lobe artifacts of much more intense DQ-DQ ridges from N_3 and N_4 nuclei.

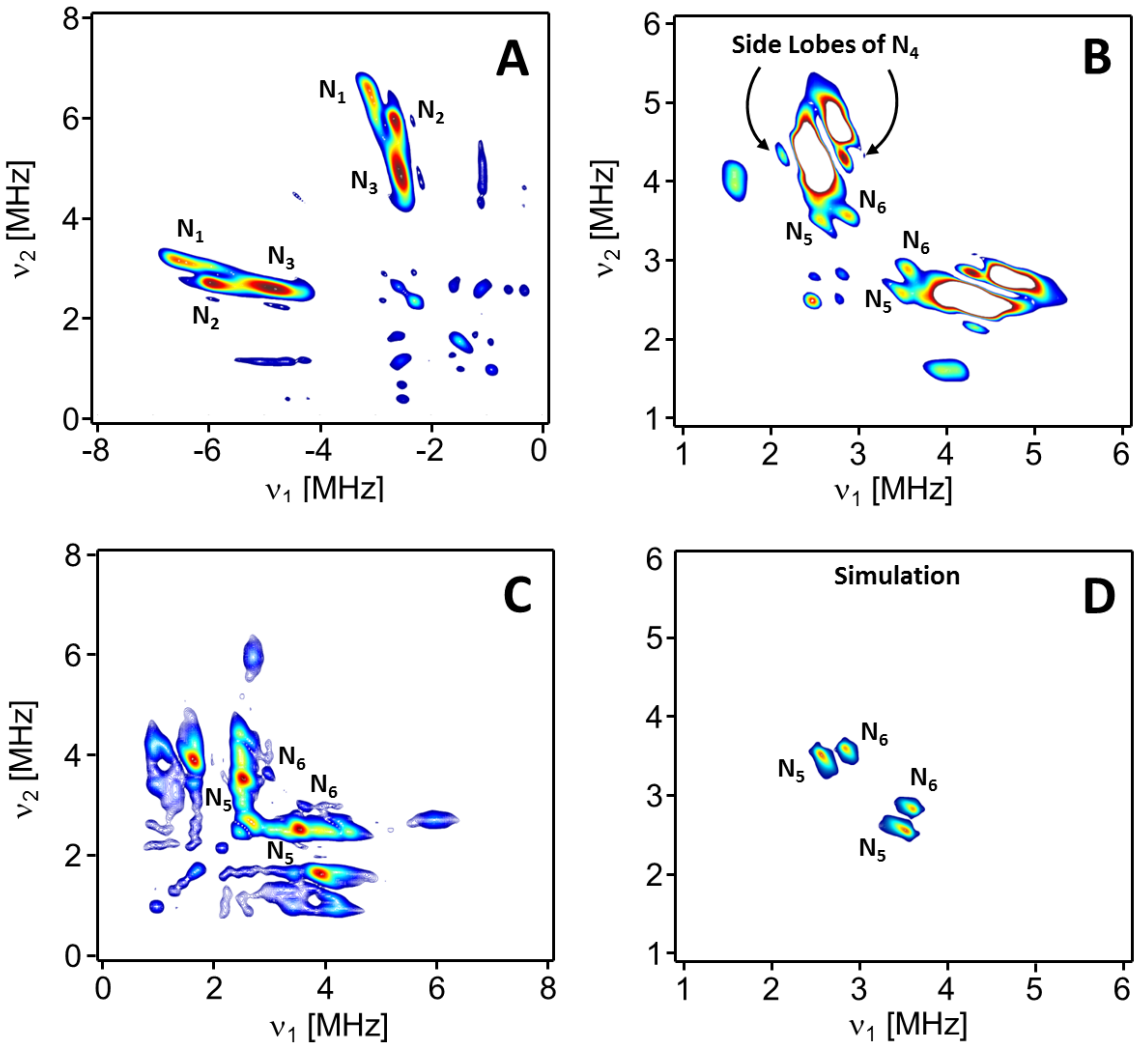

Figure 5. Selected regions of the (-,+) quadrant (**A**) and the (+,+) quadrant (**B**) of X-band 6-pulse HYSCORE spectrum of $P_{700}^{+\bullet}$ (T≈76 K) measured with inter-pulse delays of 68 ns and 120 ns between the first two and the last two microwave pulses, respectively. (**C**) Selected region of the (+,+) quadrant of the X-band 6-pulse HYSCORE spectrum of $P_{700}^{+\bullet}$ measured with inter-pulse delays of 68 ns and 234 ns between the first two and the last two microwave pulses, respectively. (**D**) Simulated HYSCORE spectrum of N_5 and N_6 nuclei.

The first possibility (*i*) could be reliably excluded because all the four features are clearly detected in the non-symmetrized spectrum, and, more importantly, are well reproduced in the 6-

pulse HYSCORE spectrum measured with 140 ns inter-pulse delays between the last two pulses (see Figure S2 of the Supplemental Information). Thus, the features are not attributed to a random noise or some pulse artifacts. The second possibility (*ii*) requires the presence of at least two rather intense additional cross-peaks for each feature having at least one of the frequency coordinates identical to those of the corresponding feature. No such or even similar cross-peaks were detected. Furthermore (*iii*), being in the DQ-DQ region, the observed features cannot be attributed to SQ or higher than DQ N_1-N_4 transitions. To confirm this, we have carried out numerical simulations, which all but failed to reproduce such features assuming only the contributions of N_1-N_4 transitions with any reasonable set of the hyperfine coupling parameters (not shown). The last possibility (*iv*) could be ruled out for the features assigned to the N_6, since the side-lobes in the HYSCORE spectrum appear as multiple, rapidly decaying images of the main signal, shifted perfectly parallel along one of the frequency axes. At least two side-lobes of the intense N_4 DQ-DQ ridge along the first frequency axis are clearly seen in the spectrum shown in Figure 5B. The features assigned to N_5 are shifted from the DQ-DQ ridges of N_4 towards lower frequencies approximately parallel to the second frequency axis, indicating a possibility that the N_5 features could be attributed to the side-lobes of the DQ-DQ ridges of N_4. In order to discriminate between the latter two possibilities, a 6-pulse HYSCORE spectrum with 234 ns delay between the last two pulses has been measured. For such a delay, the lowest frequency blind-spot appears at the location of the N_4 DQ-DQ ridges, causing a nearly complete suppression of their intensity. The corresponding spectral region of the (+,+) quadrant of the measured spectrum is shown in Figure 5C. While the overall intensity of all the spectral features decreased significantly, the N_5 ridges became the most pronounced signals in the spectral region, clearly rejecting the possibility of the features being the side lobes or induced by other

imperfections originating from the signal processing of the N_4. Unfortunately, a significantly increased effect of the pulse imperfections and a partial intensity suppression caused by a proximity to the blind spot, made the intensity of the N_6 ridges comparable to that of the noise artifacts. These effects prevented an unambiguous detection of N_6 by using this HYSCORE experiment with an extended delay (234 ns) between the last two pulses.

Once the ridges for the N_5 and N_6 nuclei have been identified, numerical simulations were employed to evaluate the corresponding parameters of the hyperfine coupling interactions. For the sake of simplicity only N_5 and N_6 were considered and the interactions with N_1-N_4 were omitted in the simulations. The simulated spectrum providing the best agreement with the experiment is shown in Figure 5D. An overlay of the experimental and simulated spectra is shown in Figure S1B (Supporting Information) and the corresponding hyperfine parameters are summarized in Table 1. As expected, while electron-nuclear hyperfine couplings are much weaker for N_5 and N_6 as compared to the N_1-N_4 nuclei, the quadrupole tensor parameters are all very similar, thus, indicating identical covalent bond structure around all the observed nitrogen nuclei.

The quadrupole and electron-nuclear hyperfine coupling parameters of the six distinct nitrogen nuclei identified by 2D HYSCORE of $P_{700}^{+\bullet}$ frozen solution samples (Table 1) agree well with those obtained previously by 1D ESEEM spectroscopy of single crystals of *PS*I.[35] Specifically, the latter experiments resolved five distinct ^{14}N nuclei all having quadrupole parameters K and η varying within narrow ranges of 0.63-0.75 MHz and 0.73-0.83, respectively. These quadrupole parameters measured by ESEEM of single crystals are identical within the experimental errors to those listed in the Table 1 and obtained in this work by HYSCORE for frozen solutions of *PS*I.

We note that even without any orientational disorder present in *PS*I solutions, the insufficient resolution owed to the 1D nature of 3-pulse ESEEM spectroscopy did not allow for accurate determination of the electron-nuclear hyperfine coupling constants and only yielded their upper limit estimates for the single crystal *PS*I samples.[35] The upper limit of 4.3 ± 0.1 MHz obtained from those ESEEM spectra also agrees well with the highest value 4.1 ± 0.2 of Table 1 (*i.e.*, $A_{\|}$ of N_1) we measured by HYSCORE.

While the 6-pulse HYSCORE has superior sensitivity towards much weaker ^{14}N hyperfine coupling interactions *vs*. the 4-pulse experiment despite of a largely decreased amplitude of the electron spin echo and a significantly increased artifacts from pulse imperfections, it also provides better resolved signals from ^{1}H nuclei. Figure 6A shows proton cross correlation signals of the 6-pulse HYSCORE spectrum measured with 68 ns inter-pulse separation between the first two pulses and 120 ns inter-pulse delay between the last two pulses (the corresponding ^{14}N signals are shown in Figures 5A and B). The spectrum clearly reveals two pairs of the ridges attributed to the two types H_1 and H_2 of stronger coupled protons. The intense unresolved feature centered at the main diagonal arises from other weakly coupled ^{1}H nuclei such as those in the solvent matrix. The ridges have a large separation within each pair, but their lengths and deviations from the anti-diagonal defined by $\nu_1 + \nu_2 = 2\nu_I$, where $\nu_I =$ 14.7 MHz (*i.e.*, the proton Larmor frequency at the magnetic field of the HYSCORE experiment), are small, indicating a large electron-nuclear coupling with a relatively small anisotropy. The linear analysis procedure[46] was then used to derive the corresponding hyperfine coupling parameters listed in Table 1.

Assignment of H_1 and H_2 in the HYSCORE spectra were made based on a comparison with the previously reported ENDOR measurements of $P_{700}^{+\bullet}$ in frozen solutions.[10] In the latter study,

the hyperfine splittings of 9.6 MHz and 7.7 MHz were observed and assigned to either $A_{\parallel}$ or $A_{\perp}$ components of the β-protons of the ring IV at the positions 17 or 18 (see Scheme 1). Thus, we tentatively assign H_1 and H_2 to either of the β -protons.

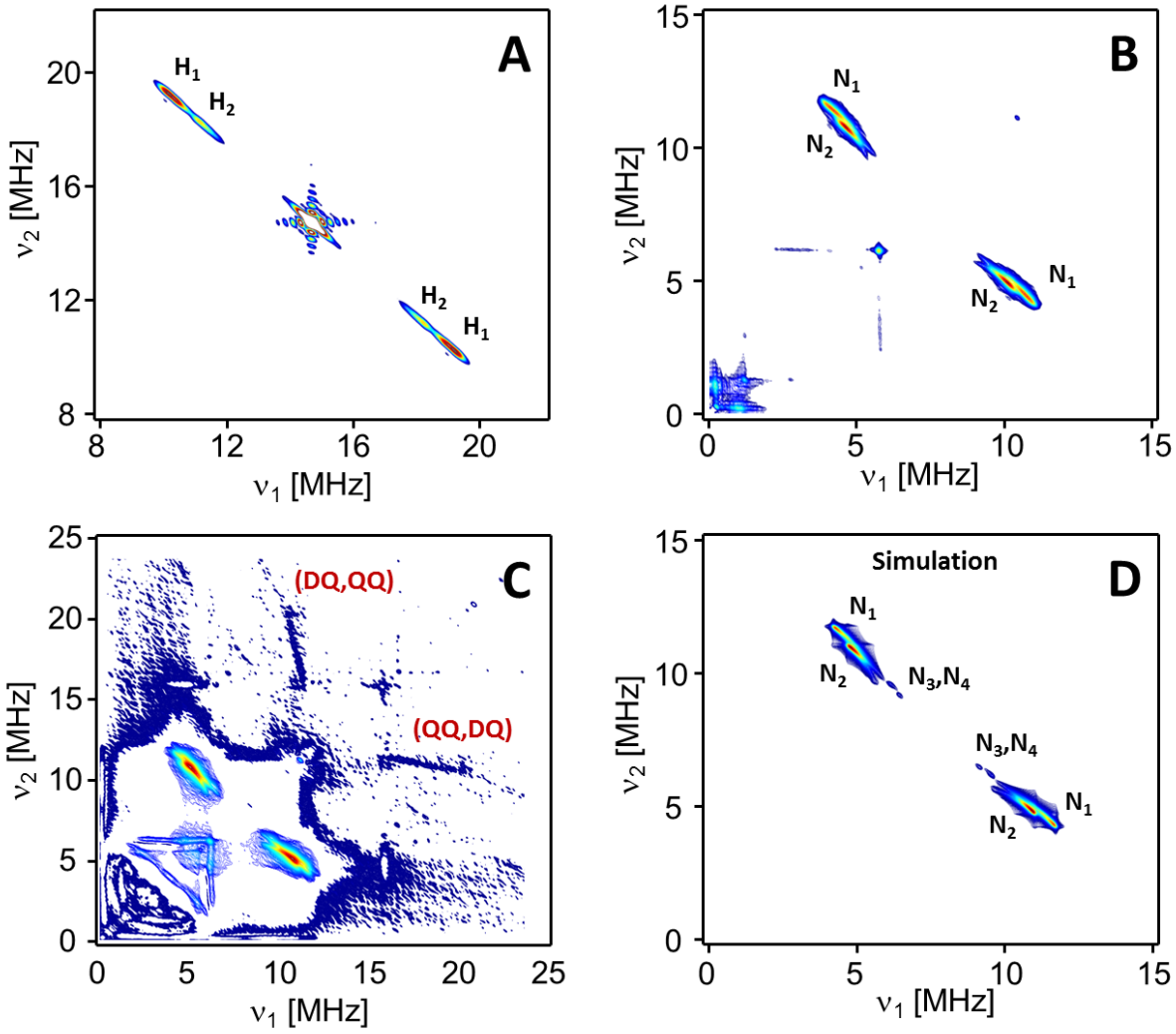

Figure 6. (**A**) X-band ^{1}H-HYSCORE spectrum (T≈76 K) obtained by using the 6-pulse sequence with 68 ns inter-pulse separation between the first two pulses and 120 ns inter-pulse delay between the last two pulses. (**B**) (+,+) Quadrant of the 4-pulse Q-band HYSCORE spectrum obtained with 140 ns separation between the first two pulses. (**C**) (+,+) Quadrant of the 6-pulse Q-band HYSCORE spectrum obtained with 68 ns inter-pulse separation between the first two

pulses and 140 ns inter-pulse delay between the last two pulses. (**D**) Simulated 4-pulse Q-band HYSCORE spectrum of N_1-N_4 nuclei when the contributions from N_5 and N_6 were neglected.

3.4. Q-Band HYSCORE of $P_{700}^{+\bullet}$

The assignment and the interpretation of the X-band (9.7 GHz) ^{14}N-HYSCORE spectra were further verified by conducting 4- and 6-pulse HYSCORE experiments with frozen solutions of $P_{700}^{+\bullet}$ at Q-band (33.8 GHz) EPR frequency. The (+,+) quadrant of the 4-pulse spectrum measured by using 140 ns separation between the first two pulses is shown in Figure 6B. The (-,+) quadrant is not shown because of the absence of cross-correlated signals. Compared to X-band, the Q-band spectrum is much "cleaner": it consists of two partially overlapping pairs of the DQ-DQ ridges, one diagonal peak corresponding to 3-pulse ESEEM frequency ν_{DQ}, barely detectable SQ-DQ ridges, and low frequency (<2 MHz) artifacts. The latter are presumably caused by the remaining imperfections of the baseline subtraction during the signal postprocessing. For a comparison, a Q-band HYSCORE spectrum simulated by using the hyperfine parameters obtained from X-band experiments and listed in Table 1 is shown in Figure 6D. For an overlay of the experimental and simulated spectra see Figure S3 of the Supporting Information section. The simulations reproduced the experimental ridges corresponding to N_1 and N_2 rather well, thus, confirming their assignment and further verifying the values of the hyperfine coupling parameters listed in Table 1.

We note that no resolved cross-peaks from N_3-N_6 could be observed in the experimental Q-band HYSCORE spectrum. While N_5 and N_6 are not expected to appear, the simulations predict the intensity of the DQ-DQ ridges of the stronger interacting N_3 and N_4 to be reduced by an order

of magnitude compared to those of N_1 and N_2 and, as such, still to be above the noise level. The failure to detect N_3 and N_4 at Q-band suggests a further drop in the DQ-DQ peaks with a decrease in hyperfine coupling *vs.* simulations, which assumed ideal excitations by the microwave pulses. Another possibility is a more pronounced destructive interference effect[52] in the experimental spectrum due to non-zero initial inter-pulse separations, corresponding to the two time coordinates of the HYSCORE experiment.

In an attempt to recover peaks corresponding to weaker hyperfine couplings, a 6-pulse Q-band HYSCORE spectrum was measured (Figure 6C). The contour levels were chosen to make the very low intensity features well pronounced: for the low intensity signals (*i.e.*, below 5% of the maximal intensity), the density of the contour levels was chosen to be 100-fold higher than for the rest of the spectrum. This uneven contour level distribution permitted for the best visual representation of the spectral features with very low intensities while avoiding the dramatic overcrowding around more intense signals. Unfortunately, no peaks from any of the N_3-N_6 nuclei were recovered by applying the 6-pulse sequence. However, partially resolved DQ-QQ peaks of N_1 and N_2 were observed. QQ frequency corresponds to simultaneous DQ transitions of the two ^{14}N nuclei. As can be seen in the Figure 5C, an extension of the DQ-QQ peaks is clearly longer than those of the DQ-DQ ridges. This serves as an indication that the axial symmetry axis of the hyperfine coupling tensors of at least N_1 and N_2 are (approximately) collinear,[53] in agreement with the hyperfine coupling parameters listed in Table 1.

3.5. Electron spin density distribution in $P_{700}^{+\bullet}$

While EPR and related double-resonance spectroscopic techniques have been long established as informative experimental methods to study electronic structure of EPR-active spin states of

photosynthetic systems, interpretation of the data for $P_{700}^{+\bullet}$ has proven to be particularly challenging because of an abundance of the nuclei magnetically coupled to the unpaired electron of the radical. Such a multitude of couplings is caused by a strong delocalization of the electron spin density over the two coupled chlorophylls and, potentially, even the surrounding amino acids. While a similar complexity has been successfully resolved for the $P_{865}^{+\bullet}$ primary donor cation radical in *Rhodopseudomonas sphaeroides* R-26 reaction center[54] and $P_{960}^{+\bullet}$ in *Rhodopseudomonas viridis*,[55] no unambiguous estimates of the electron spin density distribution among P_A and P_B halves of the P_{700} heterodimer has been successfully achieved so far. Earlier studies of $P_{700}^{+\bullet}$ by ENDOR and ESEEM have only yielded a tentative evidence of the electron spin delocalization over the two halves of the special pair.[11]

While the current HYSCORE study of frozen $P_{700}^{+\bullet}$ solutions identified electron spin density on 6 different ^{14}N nuclei *vs*. 5 nuclei observed by ESEEM,[35] an unambiguous assignment of the ^{14}N hyperfine coupling parameters is not feasible without orientation-resolved single crystal data. Alternatively, a detailed HYSCORE study of a model *Chl a* radical could potentially provide another set of useful data. Nevertheless, some important preliminary conclusions with respect to the electronic structure of the $P_{700}^{+\bullet}$ radical can be made based on the experimental data presented here.

Firstly, all the observed N_1-N_6 nuclei were tentatively assigned to six pyrrole ring nitrogen atoms of the coupled *Chl a* and *Chl a*'. There are two reasons to favor such an assignment. (*i*) All the quadrupole interaction parameters of N_1-N_6 are very similar, with only subtle differences all within experimental and/or numerical simulation errors. The close similarity between the six

quadrupole couplings becomes obvious even from a simple visual inspection of the HYSCORE spectra shown in Figures 2-5; within small deviations, all the observed DQ-DQ ridges are located in the proximity of the same curve determined by the Eqs. (1), where A is considered as a variable, and K and η are fixed parameters. The close similarity of the quadrupole couplings is strongly indicative of close similarity/identity of the chemical bonding structure involving all the observed ^{14}N nuclei. Indeed, the nuclear quadrupole interaction is determined by the electric field gradient at the position of the nucleus, which, in turn, is determined by the location of the electronic and nuclear charges in a close proximity to the nucleus. All the ^{14}N nuclei within the same *Chl* molecule belong to the pyrroles and are the parts of the same conjugated system within the molecular ring (Scheme 1). The main structural differences between the pyrrole nitrogen atoms could be caused by some variations of the electronic spin density, which is primarily located on the *p*-orbital of the nitrogen atom. For all the ^{14}N nuclei of $P_{700}^{+\bullet}$ radical, the spin density is expected not to exceed *ca*. 3% [50] and, therefore, its effect on quadrupole parameters is expected to be negligibly small, thus, justifying the assignment of the observed ^{14}N nuclei to six pyrrole ring nitrogen atoms. (*ii*) The only alternative assignment of the observed ^{14}N nuclei would be to any of the amino nitrogens belonging to the two histidine ligands, namely *His* A680 and/or *His* B660. This is, however, not probable from a theoretical perspective as no significant electron spin density is expected to be transferred to either of the *His* A680 and *His* B660 residues.[50]

Assignment of the N_1-N_6 nuclei in the HYSCORE spectra to six pyrrole ring nitrogen atoms belonging to *Chl a* and *Chl a*' moieties of the $P_{700}^{+\bullet}$ radical allows for further analysis of the electron spin density based on the observed hyperfine coupling constants summarized in Table 1. Because only four different nitrogens at the most could be from the same chlorophyll molecule,

the observed coupling constants are immediately indicative of the dimeric nature of the P700 donor with a clearly asymmetric electron spin density distribution between the two halves of $P_{700}^{+\bullet}$. This is in a full agreement with the overwhelming experimental and theoretical data all pointing to P_B carrying more spin density than P_A.[11]

The asymmetry of the spin density is typically characterized by a factor $R_{B/A}$ defined as:[50]

$$R_{B/A} = \sum_{i \in B} \rho_i \Big/ \sum_{i \in A} \rho_i \,, \qquad (2)$$

where ρ_i are the densities and the summations are carried over all the valence orbitals of the dimer halves B or A. While experimentally the individual ρ_i can be evaluated from the isotropic values of the hyperfine coupling constants, the limited number of magnetic nuclei for which these constants are measured introduces an additional error. Specifically, in this HYSCORE study we observed not all 8 but 6 ^{14}N nuclei belonging to the pyrrole rings of $P_{700}^{+\bullet}$. Moreover, the observed hyperfine coupling constants were not assigned to specific ^{14}N nuclei. Nevertheless, some initial conclusions regarding the upper limit of $R_{B/A}$ still could be deduced from the HYSCORE data. Specifically, it is easy to see that a spin density configuration with the highest $R_{B/A}$ is achieved by assigning the four largest ^{14}N hyperfine coupling constants to the nuclei of the same half of the chlorophyll dimer while the two smallest ones to the other half and assuming that the missing two ^{14}N nuclei have no spin density. One expects that an estimate of $R_{B/A}$ using just the axial hyperfine component $A_{\parallel}$ would be more accurate than based on the isotropic value $A_{iso} = \left(A_{\parallel} + 2A_{\perp}\right)/3$ because the experimental errors for twice the value of the perpendicular components (*i.e.*, errors in $2A_{\perp}$) are 5- to 10-fold higher than those for $A_{\parallel}$. Based

on $A_{\|}$ values listed in Table 1 and assuming zero spin density on the two ^{14}N nuclei of the B branch, the upper limit of the asymmetry factor is estimated as $R_{A/B}^{upper} = 7.7 \pm 0.5$ (*i.e.*, the electron spin density partitions between P_B and P_A as ≈7.7:1. If the isotropic nitrogen hyperfine coupling constants A_{iso} are considered, the upper limit of the asymmetry factor decreases to $R_{A/B}^{upper} = 7.2 \pm 1.0$. These values are likely to overestimate $R_{B/A}$ because the two ^{14}N nuclei of the B branch may still have some spin density. It is worth noting here that if one considers only the two largest A_{iso} and the two lowest A_{iso} calculated from the Table I, then $R_{A/B}^{upper} = 5.6 \pm 0.8$. The latter value is very close to the $R_{B/A} \approx 5.7$ estimate derived in the earlier reports from the experimental ENDOR and TRIPLE resonance data.[10]

A more accurate estimate of the asymmetry ratio $R_{B/A}$ could be obtained based on a tentative assignment of ^{14}N nuclei observed in the HYSCORE spectrum arising from earlier theoretical predictions of the spin density distribution over the pyrrole nitrogens.[50] According to the semiempirical molecular orbital calculations by Plato *et al.* for both P_A and P_B, only II, III, and IV nitrogen atoms of the ring (Scheme 1) carry significant spin densities leaving the ring I nitrogen with a rather small fraction. Comparing experimental data from Table 1 with the predicted ^{14}N electron-nuclear hyperfine couplings,[50] we tentatively assign the two ^{14}N groups [N_1, N_2, N_3] and [N_4, N_5, N_6] to the ring III, ring II and ring IV atoms of P_B and P_A branches, respectively. By using such an assignment and neglecting the spin density on the ring I nitrogen, the ratio of the isotropic hyperfine coupling constants derived from the Table 1 data yields $R_{B/A} = 3.1 \pm 0.5$. This value coincides within the experimental error with $R_{B/A} \approx 2.8$ predicted theoretically for the "bare" dimer[50] and $R_{B/A} \approx 2.6$ obtained more recently for the entire *PS*I

protein-pigment complex by performed large-scale QM/MM (quantum mechanics/molecular mechanics) calculations for the entire *PS*I protein-pigment complex.[56] The very recent first principles computational investigation of the spin-density asymmetry in photosynthetic reaction center models also yielded $R_{B/A}$ ranging from *ca*. 3 to 2 depending on the model and degree of truncation.[57] Specifically, it was found that an inclusion of the nearby protein environment generally leads to even more delocalized distributions and results in a decrease in $R_{B/A}$.[57] We note here that HYSCORE spectroscopy is fully applicable to investigating the distribution of electron spin density in photosynthetic reaction centers using different sample preparations including both native membranes and following a reconstitution into the membranes of specific lipid composition. Thus, such further studies could be important for understanding why, for example, the specific lipid composition of the thylakoid membranes is highly conserved among all the oxygenic photosynthetic organisms.[58]

Finally, we note that $R_{B/A} = 3.1 \pm 0.5$ obtained here from a tentative assignment of the ^{14}N HYSCORE spectra of $P_{700}^{+\bullet}$ from *Thermosynechococcus elongatus* is also comparable to the asymmetry ratio ≈2:1 measured for the primary donor cation radicals in bacterial reaction centers of *Rhodopseudomonas sphaeroides* R-26[54] and *Rhodopseudomonas viridis*.[11]

As another remark, we would like to point out that the HYSCORE data obtained in this work for two microwave bands /resonant magnetic fields allow for a comparison of sensitivities and effects of an increased magnitude of the Zeeman interaction on resolution of ^{14}N-HYSCORE spectroscopy. From a comparison of ^{14}N HYSCORE spectra of the same paramagnetic center $P_{700}^{+\bullet}$ shown in Figures 2-6, it is obvious that sensitivity of the X-band with respect to weakly coupled nuclei (*i.e.*, N_3-N_6) is dramatically higher than at Q-band. This is because the nuclear

^{14}N Zeeman interaction at Q-band is of the order of ≈3 MHz, which is significantly higher than the magnitude of the quadrupole K< 1 MHz and the half of the electron-nuclear hyperfine $A/2$< 1 MHz interactions. While higher frequency bands are more sensitive to strongly interacting nuclei and are complimentary to lower microwave frequency data, small quadrupole and electron-nuclear ^{14}N couplings are typical for biologically relevant paramagnetic species and often carry particularly valuable spectroscopic information. Thus, the authors would like to suggest developing and employing microwave frequencies below X-band to enhance HYSCORE sensitivity towards weakly coupled nuclei and, potentially, to provide important structural information not accessible by HYSCORE at X- and higher microwave frequency bands.

4. CONCLUSIONS

A combination of 4-pulse and 6-pulse HYSCORE carried out at two different microwave frequency bands (X- and Q-band) was applied to map the electron spin density distribution in the primary donor cation radical $P_{700}^{+\bullet}$ of the frozen *PS*I solution from the cyanobacterium *Thermosynechococcus elongatus*. Six distinct types of ^{14}N and two ^{1}H nuclei were resolved by this combination of the HYSCORE methods, yielding estimates of their magnetic interaction parameters such as the principal values of the electron-nuclear hyperfine coupling (^{14}N and ^{1}H) as well as quadrupole interaction tensors (for ^{14}N). All the detected ^{14}N nuclei were tentatively assigned to the pyrrole ring nitrogen atoms of the $P_{700}^{+\bullet}$ radical, indicating a delocalization of the electron spin density over both *Chl a* and *Chl a*' halves of the P700 heterodimer. While the unambiguous assignment of the detected ^{14}N nuclei primarily from the HYSCORE data would require single crystal spectra obtained at multiple crystal orientations in the magnetic field, the

spectra measured for frozen solutions permitted an estimate of the upper limit of the electron spin density asymmetry $P_{700}^{+\bullet}$ as $R_{A/B}^{upper} = 5.6 \pm 0.8$. A more reliable estimate based on a tentative assignment of ^{14}N nuclei based on the ranking and relative magnitudes of the corresponding hyperfine coupling constants obtained theoretically, yielded $R_{B/A} = 3.1 \pm 0.5$. The latter value is comparable to the asymmetry factor observed for the primary electron donor cation radical in bacterial reaction centers.

The authors expect that more precise and detailed information on the electron spin density in the $P_{700}^{+\bullet}$ radical could be obtained by applying the multi-frequency HYSCORE approach presented here to single crystals of *PS*I or the membrane reconstituted samples aligned using planar[59] or nanoporous support.[60-63] As compared to orientationally disordered frozen solutions, single crystals and/or macroscopically aligned samples are expected to provide significantly less crowded, and more importantly, orientation resolved HYSCORE spectra. This would potentially lead to improved experimental accuracy, aid in detection of still missing ^{14}N hyperfine interactions, and provide for an unambiguous assignment of the measured hyperfine coupling constants. Such an experimental approach may finally yield an accurate electron spin density map of $P_{700}^{+\bullet}$ radicals in *PS*I.

ASSOCIATED CONTENT

Supporting Information

Overlay comparison of DQ-DQ ridges of the experimental and simulated X- and Q-band HYSCORE spectra and a selected region of the (+,+) quadrant of X-band 6-pulse HYSCORE spectrum of $P_{700}^{+\bullet}$. Supporting Information is available free of charge on the ACS Publications website at DOI:

AUTHOR INFORMATION

Corresponding Author

*E-mail: Alex_Smirnov@ncsu.edu

ORCID

Alex I. Smirnov: 0000-0002-0037-2555

Melanie M. Chestnut: 0000-0003-0895-8072

Jan Kern: 0000-0002-7272-1603

Ruchira Chatterjee: 0000-0002-0865-061X

Author Contributions

The manuscript was written through contributions of all authors. All authors have given approval to the final version of the manuscript. ‖These authors contributed equally.

Funding Sources

The work at NCSU and the HYSCORE experiments were supported by U.S. DOE Contract DE-FG02-02ER15354 to AIS. EPR instrumentation at NCSU was supported by grants from the NIH (no. RR023614), the NSF (no. CHE-0840501), and NCBC (no. 2009-IDG-1015). The work at Lawrence Berkeley National Laboratory was supported by the Director, Office of Science, Office of Basic Energy Sciences (OBES), Division of Chemical Sciences, Geosciences, and Biosciences of the Department of Energy (DOE) (contract No. DE-AC02-05CH11231 (JK)

ABBREVIATIONS

*PS*I, photosystem I; EPR, electron paramagnetic resonance; ZFS, zero field splitting; HF, high frequency; ENDOR, electron nuclear double resonance; ESEEM, electron spin echo

envelope modulation; CIDNP, chemically induced dynamic nuclear polarization; FTIR, Fourier-transform infrared spectroscopy; HYSCORE, hyperfine sublevel correlation; 1D; one dimensional; 2D, two dimensional; FFT, fast Fourier transform; CW, continuous wave; SQ, single quantum; DQ, double quantum; QQ, quadrupole quantum; QM, quantum mechanics; MM, molecular mechanics.

REFERENCES

1. Golbeck, J. H., Photosystem I in Cyanobacteria. In *The Molecular Biology of Cyanobacteri.* , Bryant, D. A., Ed. Springer: Dordrecht, 1994; Vol. 1, pp 319-360.
2. Chitnis, P. R.; Xu, Q.; Chitnis, V. P.; Nechushtai, R., Function and Organization of Photosystem-I Polypeptides *Photosynthesis Res.* **1995**, *45*, 181-181.
3. Chitnis, P. R., Photosystem I. *Plant Physiol.* **1996**, *111*, 661-669.
4. Fromme, P., Structure and Function of Photosystem I. *Curr. Opin. Struct. Biol.* **1996**, *6*, 473-484.
5. Nelson, N., Photosystems and Global Effects of Oxygenic Photosynthesis. *Biochimica Et Biophysica Acta-Bioenergetics* **2011**, *1807*, 856-863.
6. Nelson, N.; Junge, W., Structure and Energy Transfer in Photosystems of Oxygenic Photosynthesis. In *Annual Review of Biochemistry, Vol 84*, Kornberg, R. D., Ed. 2015; Vol. 84, pp 659-683.
7. Golbeck, J. H., *Photosystem I. The Light-Driven Plastocyanin: Ferredoxin Oxidoreductase*. 1 ed.; Springer Netherlands: 2006; p 713.
8. Chitnis, P. R., Photosystem I: Function and Physiology. *Annu. Rev. Plant Physiol. Plant Mol. Biol.* **2001**, *52*, 593-626.
9. Srinivasan, N.; Golbeck, J. H., Protein-Cofactor Interactions in Bioenergetic Complexes: The Role of the a(1a) and a(1b) Phylloquinones in Photosystem I. *Biochimica Et Biophysica Acta-Bioenergetics* **2009**, *1787*, 1057-1088.
10. Kass, H.; Fromme, P.; Witt, H. T.; Lubitz, W., Orientation and Electronic Structure of the Primary Donor Radical Cation P-700(+Center Dot) in Photosystem I: A Single Crystals Epr and Endor Study. *J. Phys. Chem. B* **2001**, *105*, 1225-1239.
11. Webber, A. N.; Lubitz, W., P700: The Primary Electron Donor of Photosystem I. *Biochimica Et Biophysica Acta-Bioenergetics* **2001**, *1507*, 61-79.
12. Muller, M. G.; Niklas, J.; Lubitz, W.; Holzwarth, A. R., Ultrafast Transient Absorption Studies on Photosystem I Reaction Centers from Chlamydomonas Reinhardtii. 1. A New Interpretation of the Energy Trapping and Early Electron Transfer Steps in Photosystem I. *Biophys. J.* **2003**, *85*, 3899-3922.
13. Holzwarth, A. R.; Muller, M. G.; Niklas, J.; Lubitz, W., Ultrafast Transient Absorption Studies on Photosystem I Reaction Centers from Chlamydomonas Reinhardtii. 2: Mutations near the P700 Reaction Center Chlorophylls Provide New Insight into the Nature of the Primary Electron Donor. *Biophys. J.* **2006**, *90*, 552-565.
14. Ptushenko, V. V.; Cherepanov, D. A.; Krishtalik, L. I.; Semenov, A. Y., Semi-Continuum Electrostatic Calculations of Redox Potentials in Photosystem I. *Photosynthesis Res.* **2008**, *97*, 55-74.
15. Muller, M. G.; Slavov, C.; Luthra, R.; Redding, K. E.; Holzwarth, A. R., Independent Initiation of Primary Electron Transfer in the Two Branches of the Photosystem I Reaction Center. *Proceedings of the National Academy of Sciences of the United States of America* **2010**, *107*, 4123-4128.
16. Di Donato, M.; Stahl, A. D.; van Stokkum, I. H. M.; van Grondelle, R.; Groot, M. L., Cofactors Involved in Light-Driven Charge Separation in Photosystem I Identified by Subpicosecond Infrared Spectroscopy. *Biochemistry* **2011**, *50*, 480-490.

17. Molotokaite, E.; Remelli, W.; Casazza, A. P.; Zucchelli, G.; Polli, D.; Cerullo, G.; Santabarbara, S., Trapping Dynamics in Photosystem I-Light Harvesting Complex I of Higher Plants Is Governed by the Competition between Excited State Diffusion from Low Energy States and Photochemical Charge Separation. *J. Phys. Chem. B* **2017**, *121*, 9816-9830.
18. Cherepanov, D. A.; Shelaev, I. V.; Gostev, F. E.; Mamedov, M. D.; Petrova, A. A.; Aybush, A. V.; Shuvalov, V. A.; Semenov, A. Y.; Nadtochenko, V. A., Mechanism of Adiabatic Primary Electron Transfer in Photosystem I: Femtosecond Spectroscopy Upon Excitation of Reaction Center in the Far-Red Edge of the Qy Band. *Biochimica Et Biophysica Acta-Bioenergetics* **2017**, *1858*, 895-905.
19. Zamzam, N.; Kaucikas, M.; Nurnberg, D. J.; Rutherford, A. W.; van Thor, J. J., Femtosecond Infrared Spectroscopy of Chlorophyll F-Containing Photosystem I. *PCCP* **2019**, *21*, 1224-1234.
20. Jordan, P.; Fromme, P.; Witt, H. T.; Klukas, O.; Saenger, W.; Krauss, N., Three-Dimensional Structure of Cyanobacterial Photosystem I at 2.5 Angstrom Resolution. *Nature* **2001**, *411*, 909-917.
21. Frank, H. A.; McLean, M. B.; Sauer, K., Triplet-States in Photosystem-I of Spinach-Chloroplasts and Sub-Chloroplast Particles, *Proceedings of the National Academy of Sciences of the United States of America* **1979**, *76*, 5124-5128.
22. Setif, P.; Brettel, K., Photosystem-I Photochemistry under Highly Reducing Conditions - Study of the P700 Triplet-State Formation from the Secondary Radical Pair ($P700^{+}$-A_1^{-}). *Biochim. Biophys. Acta* **1990**, *1020*, 232-238.
23. Budil, D. E.; Thurnauer, M. C., The Chlorophyll Triplet-State as a Probe of Structure and Function in Photosynthesis. *Biochim. Biophys. Acta* **1991**, *1057*, 1-41.
24. Denblanken, H. J.; Hoff, A. J., High-Resolution Absorbance-Difference Spectra of the Triplet-State of the Primary Donor P-700 in Photosystem-I Subchloroplast Particles Measured with Absorbance-Detected Magnetic-Resonance at 1.2 K - Evidence That P-700 Is a Dimeric Chlorophyll Complex. *Biochim. Biophys. Acta* **1983**, *724*, 52-61.
25. Vrieze, J.; Gast, P.; Hoff, A. J., Structure of the Reaction Center of Photosystem I of Plants. An Investigation with Linear-Dichroic Absorbance-Detected Magnetic Resonance. *J. Phys. Chem.* **1996**, *100*, 9960-9967.
26. Poluektov, O. G.; Utschig, L. M.; Schlesselman, S. L.; Lakshmi, K. V.; Brudvig, G. W.; Kothe, G.; Thurnauer, M. C., Electronic Structure of the P-700 Special Pair from High-Frequency Electron Paramagnetic Resonance Spectroscopy. *J. Phys. Chem. B* **2002**, *106*, 8911-8916.
27. Bratt, P. J.; Rohrer, M.; Krzystek, J.; Evans, M. C. W.; Brunel, L. C.; Angerhofer, A., Submillimeter High-Field Epr Studies of the Primary Donor in Plant Photosystem I P700. *J. Phys. Chem. B* **1997**, *101*, 9686-9689.
28. Zech, S. G.; Hofbauer, W.; Kamlowski, A.; Fromme, P.; Stehlik, D.; Lubitz, W.; Bittl, R., A Structural Model for the Charge Separated State P(700)(Center Dot+)a(1)(Center Dot-) in Photosystem I from the Orientation of the Magnetic Interaction Tensors. *J. Phys. Chem. B* **2000**, *104*, 9728-9739.
29. Teutloff, C.; Hofbauer, W.; Zech, S. G.; Stein, M.; Bittl, R.; Lubitz, W., High-Frequency Epr Studies on Cofactor Radicals in Photosystem I. *Appl. Magn. Reson.* **2001**, *21*, 363-379.
30. Bratt, P. J.; Poluektov, O. G.; Thurnauer, M. C.; Krzystek, J.; Brunel, L. C.; Schrier, J.; Hsiao, Y. W.; Zerner, M.; Angerhofer, A., The *g*-Factor Anisotropy of Plant Chlorophyll $A^{\cdot+}$. *J. Phys. Chem. B* **2000**, *104*, 6973-6977.

31. Petrenko, A.; Maniero, A. L.; van Tol, J.; MacMillan, F.; Li, Y. J.; Brunel, L. C.; Redding, K., A High-Field EPR Study of $P_{700}^{+\cdot}$ In Wild-Type and Mutant Photosystem I from *Chlamydomonas Reinhardtii*. *Biochemistry* **2004**, *43*, 1781-1786.
32. Lubitz, W., Photochemical Processes in Photosynthesis Studied by Advanced Electron Paramagnetic Resonance Techniques. *Pure Appl. Chem.* **2003**, *75*, 1021-1030.
33. Bittl, R.; Zech, S. G., Pulsed Epr Study of Spin-Coupled Radical Pairs in Photosynthetic Reaction Centers: Measurement of the Distance between and in Photosystem I and between and in Bacterial Reaction Centers. *The Journal of Physical Chemistry B* **1997**, *101*, 1429-1436.
34. Käss, H. Die Struktur Des Primären Donators in Photosystem I. PhD, Technische Universität, Berlin, 1995.
35. Kass, H.; Fromme, P.; Lubitz, W., Quadrupole Parameters of Nitrogen Nuclei in the Cation Radical P-700(•+) Determined by ESEEM of Single Crystals of Photosystem I. *Chem. Phys. Lett.* **1996**, *257*, 197-206.
36. Diller, A.; Roy, E.; Gast, P.; van Gorkom, H. J.; de Groot, H. J. M.; Glaubitz, C.; Jeschke, G.; Matysik, J.; Alia, A., N-15 Photochemically Induced Dynamic Nuclear Polarization Magic-Angle Spinning Nmr Analysis of the Electron Donor of Photosystem Ii. *Proceedings of the National Academy of Sciences of the United States of America* **2007**, *104*, 12767-12771.
37. Najdanova, M.; Janssen, G. J.; de Groot, H. J. M.; Matysik, J.; Alia, A., Analysis of Electron Donors in Photosystems in Oxygenic Photosynthesis by Photo-CIDNP Mas NMR. *Journal of Photochemistry and Photobiology B-Biology* **2015**, *152*, 261-271.
38. Breton, J.; Nabedryk, E.; Leibl, W., Ftir Study of the Primary Electron Donor of Photosystem I (P700) Revealing Delocalization of the Charge in P700(+) and Localization of the Triplet Character in (3)P700. *Biochemistry* **1999**, *38*, 11585-11592.
39. Wang, R. L.; Sivakumar, V.; Li, Y. J.; Redding, K.; Hastings, G., Mutation Induced Modulation of Hydrogen Bonding to P700 Studied Using Ftir Difference Spectroscopy. *Biochemistry* **2003**, *42*, 9889-9897.
40. Alia; Roy, E.; Gast, P.; van Gorkom, H. J.; de Groot, H. J. M.; Jeschke, G.; Matysik, J., Photochemically Induced Dynamic Nuclear Polarization in Photosystem I of Plants Observed by C-13 Magic-Angle Spinning NMR. *J. Am. Chem. Soc.* **2004**, *126*, 12819-12826.
41. Hastings, G.; Ramesh, V. M.; Wang, R.; Sivakumar, V.; Webber, A., Primary Donor Photo-Oxidation in Photosystem I: A Re-Evaluation of (P700+ − P700) Fourier Transform Infrared Difference Spectra. *Biochemistry* **2001**, *40*, 12943-12949.
42. Höfer, P.; Grupp, A.; Nebenführ, H.; Mehring, M., Hyperfine Sublevel Correlation (Hyscore) Spectroscopy: A 2D ESR Investigation of the Squaric Acid Radical. *Chem. Phys. Lett.* **1986**, *132*, 279-282.
43. Kasumaj, B.; Stoll, S., 5-and 6-Pulse Electron Spin Echo Envelope Modulation (ESEEM) of Multi-Nuclear Spin Systems. *J. Magn. Reson.* **2008**, *190*, 233-247.
44. Kern, J.; Loll, B.; Luneberg, C.; DiFiore, D.; Biesiadka, J.; Irrgang, K. D.; Zouni, A., Purification, Characterisation and Crystallisation of Photosystem Ii from Thermosynechococcus Elongatus Cultivated in a New Type of Photobioreactor. *Biochimica Et Biophysica Acta-Bioenergetics* **2005**, *1706*, 147-157.
45. Stoll, S.; Schweiger, A., Easyspin, a Comprehensive Software Package for Spectral Simulation and Analysis in EPR. *J. Magn. Reson.* **2006**, *178*, 42-55.
46. Chatterjee, R.; Milikisiyants, S.; Coates, C. S.; Lakshmi, K. V., High-Resolution Two-Dimensional H-1 and N-14 Hyperfine Sublevel Correlation Spectroscopy of the Primary Quinone of Photosystem Ii. *Biochemistry* **2011**, *50*, 491-501.

47. Golbeck, J. H., Structure and Function of Photosystem-I. *Annu. Rev. Plant Physiol. Plant Mol. Biol.* **1992**, *43*, 293-324.
48. Deligiannakis, Y.; Louloudi, M.; Hadjiliadis, N., Electron Spin Echo Envelope Modulation (Eseem) Spectroscopy as a Tool to Investigate the Coordination Environment of Metal Centers. *Coord. Chem. Rev.* **2000**, *204*, 1-112.
49. Flanagan, H. L.; Singel, D. J., Analysis of ^{14}N ESEEM Patterns of Randomly Oriented Solids. *J. Chem. Phys.* **1987**, *87*, 5606-5616.
50. Plato, M.; Krauß, N.; Fromme, P.; Lubitz, W., Molecular Orbital Study of the Primary Electron Donor P700 of Photosystem I Based on a Recent X-Ray Single Crystal Structure Analysis. *Chem. Phys.* **2003**, *294*, 483-499.
51. Prisner, T. F.; McDermott, A. E.; Un, S.; Norris, J. R.; Thurnauer, M. C.; Griffin, R. G., Measurement of the g-Tensor of the P700+. Signal from Deuterated Cyanobacterial Photosystem I Particles. *Proc Natl Acad Sci U S A* **1993**, *90*, 9485-8.
52. Dikanov, S. A.; Tyryshkin, A. M.; Bowman, M. K., Intensity of Cross-Peaks in HYSCORE Spectra of S=1/2, I=1/2 Spin Systems. *J. Magn. Reson.* **2000**, *144*, 228-242.
53. Liesum, L.; Schweiger, A., Multiple Quantum Coherence in HYSCORE Spectra. *J. Chem. Phys.* **2001**, *114*, 9478-9488.
54. Lendzian, F.; Huber, M.; Isaacson, R. A.; Endeward, B.; Plato, M.; Bönigk, B.; Möbius, K.; Lubitz, W.; Feher, G., The Electronic Structure of the Primary Donor Cation Radical in Rhodobacter Sphaeroides R-26: ENDOR and Triple Resonance Studies in Single Crystals of Reaction Centers. *Biochimica et Biophysica Acta (BBA) - Bioenergetics* **1993**, *1183*, 139-160.
55. Lendzian, F.; Lubitz, W.; Scheer, H.; Hoff, A. J.; Plato, M.; Tränkle, E.; Möbius, K., Esr, Endor and Triple Resonance Studies of the Primary Donor Radical Cation P960+• in the Photosynthetic Bacterium Rhodopseudomonas Viridis. *Chem. Phys. Lett.* **1988**, *148*, 377-385.
56. Saito, K.; Ishikita, H., Cationic State Distribution over the P700 Chlorophyll Pair in Photosystem I. *Biophys. J.* **2011**, *101*, 2018-2025.
57. Artiukhin, D. G.; Eschenbach, P.; Neugebauer, J., Computational Investigation of the Spin-Density Asymmetry in Photosynthetic Reaction Center Models from First Principles. *The Journal of Physical Chemistry B* **2020**, *124*, 4873-4888.
58. Kobayashi, K.; Endo, K.; Wada, H., Specific Distribution of Phosphatidylglycerol to Photosystem Complexes in the Thylakoid Membrane. *Frontiers in Plant Science* **2017**, *8*.
59. Rutherford, A. W., Orientation of EPR Signals Arising from Components in Photosystem Ii Membranes. *Biochimica et Biophysica Acta (BBA) - Bioenergetics* **1985**, *807*, 189-201.
60. Smirnov, A. I.; Poluektov, O. G., Substrate-Supported Lipid Nanotube Arrays. *J. Am. Chem. Soc.* **2003**, *125*, 8434-8435.
61. Chekmenev, E. Y.; Hu, J.; Gor'kov, P. L.; Brey, W. W.; Cross, T. A.; Ruuge, A.; Smirnov, A. I., ^{15}N and ^{31}P Solid-State Nmr Study of Transmembrane Domain Alignment of M2 Protein of Influenza a Virus in Hydrated Cylindrical Lipid Bilayers Confined to Anodic Aluminum Oxide Nanopores. *J. Magn. Reson.* **2005**, *173*, 322-327.
62. Chekmenev, E. Y.; Gor'kov, P. L.; Cross, T. A.; Alaouie, A. M.; Smirnov, A. I., Flow-through Lipid Nanotube Arrays for Structure-Function Studies of Membrane Proteins by Solid-State NMR Spectroscopy. *Biophys. J.* **2006**, *91*, 3076-3084.
63. Marek, A.; Tang, W.; Milikisiyants, S.; Nevzorov, A A.; Smirnov, A I., Nanotube Array Method for Studying Lipid-Induced Conformational Changes of a Membrane Protein by Solid-State NMR. *Biophysical J.* **2015**, *108*, 5-9.

TOC

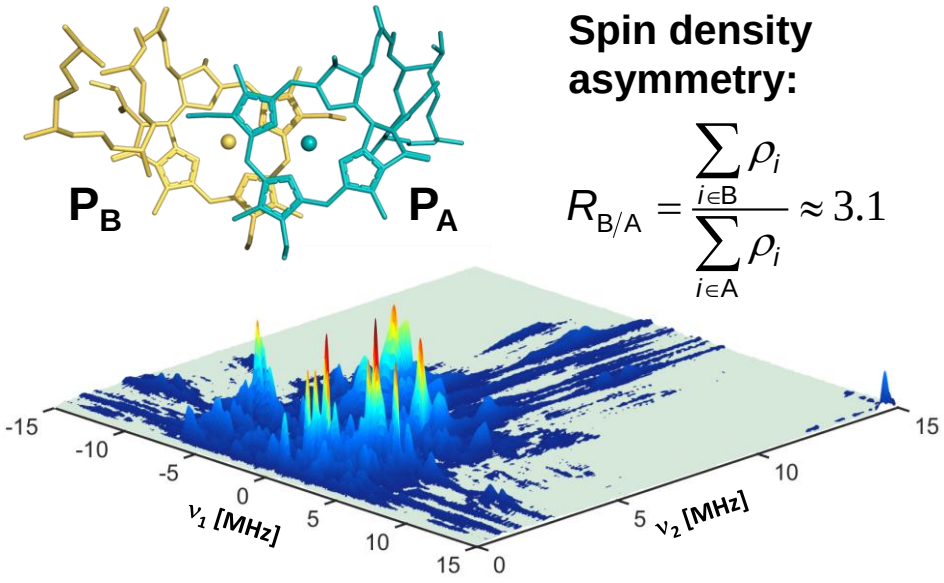
P_B
P_A
Spin density asymmetry:
$R_{B/A} = \frac{\sum_{i \in B} \rho_i}{\sum_{i \in A} \rho_i} \approx 3.1$
-15
-10
-5
0
5
10
15
ν1 [MHz]
0
5
10
15
ν2 [MHz]